Topological Properties of the Lowest Landau Level: A Study of Chern Number Statistics

Edward Deleu

Advised by Professor Ravindra N. Bhatt

April 29, 2025

Abstract

A two-dimensional system of non-interacting electrons confined to the lowest Landau level (LLL) under a strong perpendicular magnetic field and a Gaussian white-noise random potential is investigated. Extended states are known to carry quantized Hall current and are associated with a nonzero Chern number, a topological invariant that encodes a wavefunction's sensitivity to changes in boundary condition. In contrast, localized states have zero Chern number and confined wavefunctions. While the Chern number offers a topological perspective on localization, Random Matrix Theory (RMT) provides a statistical viewpoint on ensembles of random matrices confined to certain symmetry classes. The statistical connections between Chern numbers and spectral properties of random matrices are explored in this report for systems up to $N_\phi = 2048$ states. The level spacing statistics demonstrate a clear transition from Gaussian Unitary Ensemble behavior at the band center to Poisson statistics at the band edges. However, filtering eigenvalues by their Chern character at the band center reveals more complex behavior: level spacings between states of identical Chern number display intermediate statistics, influenced by the presence of interspersed states with different Chern character and the level repulsions between extended states.

Submitted in partial fulfillment of the requirements for the degree of Bachelor of Science in Engineering, Department of Electrical and Computer Engineering, Princeton University.

I hereby declare that this Independent Work report does not include regulated human subjects research or regulated animal subjects research. I hereby declare that this Independent Work report represents my own work in accordance with University regulations. */s/ Edward Deleu*

Contents

1 Introduction **3**

2 Theoretical Framework **6**

3 Methods **9**

3.1 Random Potential 11

3.2 Hamiltonian Computations 12

3.3 Chern Number Computation 13

3.4 Chern Number Convergence 15

4 Chern State Characterization **18**

5 Level Spacing Statistics **21**

6 Level Spacing Ratio Analysis **26**

7 Conclusion **31**

A Extended Analysis of Level Spacings **33**

A.1 Varying Window Sizes for $N_\phi = 2048$ 33

A.2 Separation Analysis for $N_\phi = 1024$ 35

B Extended Analysis of Level Spacing Ratios **38**

1 Introduction

The classical Hall effect was discovered in 1879 by Edwin Hall. It describes the transverse voltage produced in an electrical conductor carrying a longitudinal current subject to a perpendicular magnetic field [1]. This phenomenon arises due to the Lorentz force acting on moving charge carriers, causing the carriers to accumulate on one side of the conductor [2]. This accumulation leads to an electric field that opposes further charge separation by the Lorentz force, resulting in the so-called Hall voltage. While this effect is fundamental in understanding two-dimensional systems subject to magnetic fields, the original theory fails to explain many experimentally observed phenomena [2]. A century later in 1980, Klaus von Klitzing discovered that the Hall resistance exhibited quantized behavior while studying a two-dimensional electron gas in a Silicon MOSFET at low-temperatures and high magnetic-fields [3]. He discovered that the Hall resistance is quantized according to $R_H = \frac{h}{ie^2}$ where i is an integer, h is Planck's constant, and e is the fundamental unit of charge [4]. This is known simply as the integer quantum Hall effect.

The quantum Hall effect has been subject to extensive study over the past four decades. In a two-dimensional electron gas subject to a perpendicular magnetic-field, the quantum states organize into extensively degenerate, quantized Landau levels. In the presence of disorder in the form of a random potential, the levels broaden and mix. The gap between Landau levels widens as the magnetic field strength increases. Considering a system in the high magnetic field limit with sufficiently low thermal energy compared to the Landau level spacing, it is sufficient to consider only the lowest Landau level (LLL) for study [5, 6]. For this system, one may make the distinction between localized and extended states. A localized state has a wavefunction confined to a finite region in space, outside of which the wavefunction exponentially decays [7]. These localized states arise as a consequence of disorder or impurities in a sample: due to the confinement, localized states may not conduct any Hall current [8, 7, 9]. In contrast, an extended state has a wavefunction spread out across a sample and may subsequently carry Hall current [7, 6, 10]. The distinction may also be made based on the sensitivity of a wavefunction's nodes to continuous changes in boundary conditions: an extended state has a wavefunction that may be made to vanish at any given location in real-space by an appropriate choice of boundary conditions, while localized states are confined regardless of choice in boundary conditions [6, 1].

The average Hall conductivity for an eigenstate over all boundary condition angles has been found to necessarily be an integer multiple of e^2/h, where the integer is precisely the first Chern index $C(m)$ [11, 12]. The Chern number is a topological invariant which characterizes the topological properties of a state's wavefunctions [10]. Thus, the connection has been drawn that the Chern number is a measure of a state's capacity to carry Hall current. Only states with non-zero Chern number may carry Hall current and hence contribute to the Hall conductivity. This is also connected to the localization and extent of a state: states with non-zero Chern number are extended and may transport charge, while states with zero Chern number are localized [10]. In this problem, Chern number hence describes the sensitivity of the nodes of a wavefunctions to changes in the boundary conditions: states with $C \neq 0$ are extended and have nodes that may be moved, while states with $C = 0$ have confined nodes and are localized [6].

Extended states concentrate at the center of broadened Landau levels [4, 13, 1]. In the quantum Hall effect, plateaus of Hall (transverse) conductivity occur while a system's Fermi energy lies within a region of localized states. Small changes in energy will not change the number of conducting states, leading to the quantized Hall conductance. An increase in Fermi energy near the extended states, however, will yield an increase in the Hall conductivity [11, 4]. In terms of the magnetic field, increasing the field strength increases the degeneracy (number of available quantum states) per Landau level; there are then fewer filled levels and less filled extended states, thereby leading to a higher Hall resistance. Prior numerical studies of finite systems have shown that the band of extended states narrows as the number of states increases, such that all extended states collapse to a single critical energy in the thermodynamic limit $N_\phi \to \infty$ [10]. Extensive efforts have focused on determining the exact relationship for the localization length ξ through numerical simulations with various methodologies: the localization length diverges with a power-law relationship $\xi \sim |E - E_c|^{-\nu}$ where E_c is the center of the LLL in the electron-hole symmetric scenario and ν is the localization length exponent [10, 13].

While the topological Chern number provides one lens from which this localization problem may be viewed, Random Matrix Theory (RMT) provides yet another angle from which this system may be analyzed. RMT was originally introduced to describe the statistical properties of energy levels in atomic nuclei, and it has since been used in countless applications in physics [14, 15].

In brief, it describes the statistical behavior of the eigenvalue spectra of matrices whose entries are independent random variables constrained by certain symmetry classes. A key property of the theory is universality: regardless of the exact details of a system, a matrix's eigenvalues will follow certain statistics and distributions falling into the universal classes solely dependent on the exact symmetry conditions [14]. The level spacing distributions predicted by RMT follow Wigner–Dyson statistics which are approximated using the so-called Wigner surmise: this is a generalized formula for the probability in level spacing distributions, originally derived for 2×2 random matrices [14]. However, these translate quite well to ensembles of larger matrices [14]. The three fundamental matrix ensembles of RMT are the Gaussian orthogonal ensemble (GOE), the Gaussian unitary ensemble (GUE), and the Gaussian symplectic ensemble (GSE). The GUE is of particular interest for this work involving magnetic fields, as it applies to complex Hermitian matrices of systems breaking time reversal symmetry [16]. A hallmark of RMT is the presence of level repulsions: the eigenvalues of random matrices tend to be highly correlated and repel one another [16].

In general, eigenvalues that are uncorrelated (statistically independent) and random will follow Poisson statistics [17, 16]. These eigenvalues will have no level repulsion, so it's statistically possible to find two eigenvalues arbitrarily close to one another where the separation s generally follows the probability $P(s) = e^{-s}$ [17]. In the presence of zero disorder for the quantum Hall problem, all states are delocalized and should follow GUE statistics since the Hamiltonian is a random complex Hermitian matrix [18]. However, the presence of disorder spatially localizes states. These localized states will directly follow Poisson statistics: their wavefunctions are tightly confined in space, and they are unlikely to overlap and will hence have negligible interactions with one another [17, 5]. In contrast, extended states are delocalized across a system, allowing for their wavefunctions to significantly overlap and influence one another. Extended states should follow Wigner-Dyson statistics– in specific, GUE statistics with $P(s) = (32/\pi^2)s^2 \exp[-4s^2/\pi]$ [16, 17, 5]. Notably, the probability vanishes as $s \to 0$, indicating strong level repulsion. Fundamentally, level repulsions arise due to non-zero off-diagonal matrix terms that lead nearby energies to repel and avoid crossing. Conversely, matrix elements without these off-diagonal terms may have an actual crossing and will not have the repulsion, leading to the Poisson statistics. The presence of disorder in the quantum Hall system leads to this complex landscape and mixture of statistical

properties.

The connection between topological properties and the RMT based statistics of level spacings remain relatively unexplored for this quantum Hall system. This work seeks to investigate these relationships, quantitatively determining the effects of Chern number on the statistics and distributions of energy spectra. By analyzing large ensembles of disordered LLL Hamiltonian matrices across a wide range of system sizes, this work aims to characterize the connection between topology and spectral behavior.

2 Theoretical Framework

Consider the case of a two-dimensional system of non-interacting electrons with size $L \times L$ under a perpendicular magnetic field B and a random Gaussian white-noise potential. Generally, the Hamiltonian may be written as:

$$H = H_0 + V(\mathbf{r}) = \frac{1}{2m}(\mathbf{P} + \frac{e}{c}\mathbf{A})^2 + V(\mathbf{r}) \tag{1}$$

where $V(\mathbf{r})$ is the random potential, $\mathbf{P}$ is the canonical momentum operator, and the symmetric gauge $\mathbf{A} = \frac{1}{2}B(y, -x)$ is used [13]. For a free particle, H_0 is the harmonic oscillator Hamiltonian with energy spectrum $E_n = (n + \frac{1}{2})\hbar\omega_c$ where the cyclotron frequency is $\omega_c = eB/mc$ [6]. Each Landau level will have a degenerate number of states given by $N_\phi = \frac{L^2}{2\pi\ell_b^2}$ where the magnetic length is $\ell_b = \sqrt{\frac{\hbar c}{eB}}$. Equivalently, N_ϕ may be considered as the number of flux quanta through the system, $N_\phi = \frac{BL^2}{\Phi_o}$ where one quantum of flux is $\Phi_o = \frac{2\pi\hbar}{e}$ [1]. Various system sizes will be considered: the magnetic field strength is considered to be fixed such that scaling the system size directly corresponds to scaling the area of the sample.

With a sufficiently high magnetic field the entire problem may be described as projected into the LLL without loss of generality, assuming that the widening of the Landau levels from the random potential is less than the inter-Landau level spacing [6, 19]. A Landau-like strip basis $|\phi_m\rangle$ may be

constructed by requiring

$$\begin{cases} t_1|\phi_m\rangle = |\phi_{m+1}\rangle \\ t_2|\phi_m\rangle = e^{i\frac{2\pi m}{N_\phi}}|\phi_m\rangle \end{cases} \tag{2}$$

for two primitive translation operators t_1 and t_2 where the basis functions are periodic in $m \to m + N_\phi$ [13]. The random potential may be projected into the lowest Landau level such that,

$$\tilde{V} = \sum_{j,k} |\phi_j\rangle\langle\phi_j| \sum_{\mathbf{q}} V_{\mathbf{q}} e^{i\mathbf{q}\cdot\mathbf{r}} |\phi_k\rangle\langle\phi_k|, \tag{3}$$

where j, k label basis states, $\mathbf{q} = (2\pi m/L_x, 2\pi n/L_y)$ with integers m, n, and $V_{\mathbf{q}}$ are the Fourier coefficients of the random potential. The Gaussian white-noise potential is considered, which has the correlation functions $\langle V(\mathbf{r})\rangle = 0$ and $\langle V(\mathbf{r_1})V(\mathbf{r_2})\rangle = V^2\delta(\mathbf{r_1} - \mathbf{r_2})$ where V is the potential strength [19]. The potential is uncorrelated in real-space and has electron-hole symmetry. The random potential is defined over the $L \times L$ sample and is periodically extended to fill the entire plane. Generalized periodic boundary conditions may be imposed for this $L_x = L_y = L$ square sample by requiring all eigenstates $|\psi(\vec{\theta})\rangle$ to be simultaneous eigenstates of two magnetic translation operators,

$$t(\mathbf{L_j})|\psi(\vec{\theta})\rangle = e^{i\theta_j}|\psi(\vec{\theta})\rangle,\ j = x, y, \tag{4}$$

with twist angle $\vec{\theta} = (\theta_x, \theta_y)$ where $\theta_j \in [0, 2\pi]$ and $t(\mathbf{r})$ is the magnetic translation operator [10, 13]. This is effectively equivalent to periodically tiling the $L \times L$ sample over all space, or alternatively considering the wavefunctions to lie on a square torus. Then, the exact Hamiltonian matrix may be calculated by:

$$H_{jk}(\theta_x, \theta_y) = \sum_{m,n} V_{mn} e^{-\frac{\pi}{N_\phi}(\frac{m^2+n^2}{2}+i\pi mn)} e^{i\frac{m\theta_y}{N_\phi}} e^{-i\frac{n\theta_x}{N_\phi}} e^{-i\frac{2\pi mj}{N_\phi}} \langle\phi_j|\phi_{k-n}\rangle \tag{5}$$

where j, k index the Hamiltonian matrix running from 1 to N_ϕ inclusive, m, n index the potential matrix of Fourier coefficients, and $\theta_x, \theta_y \in [0, 2\pi]$ are free parameters that impose the boundary conditions. The entire Hamiltonian calculation is presented as derived by Zhu et. al which covers the operators and derivation in more depth [13]. With this construction, the overlap $\langle\phi_j|\phi_{k-n}\rangle$ is unity for $(j - (k - n) \bmod N_\phi = 0$ and zero otherwise. With the electron-hole symmetric random

potential, the critical energy is expected to be at the band center $E_c = 0$ [13].

Hall conductivity σ_{xy} may be given as a function of both energy E and the boundary condition twist angles θ_x, θ_y. For brevity, the mth eigenstate may equivalently be written as $|m\rangle \equiv |\psi_m(\vec{\theta})\rangle$. The Kubo formula for non-interacting electrons can be written as a sum over the eigenstates,

$$\sigma_{xy}(E;\theta_x;\theta_y) = \sum_{m=1}^{N_\phi} \delta\sigma_{xy}(m;\theta_x;\theta_y)\Theta(E - E_m), \tag{6}$$

where

$$\delta\sigma_{xy}(m;\theta_x;\theta_y) = i\frac{e^2}{\hbar}\left(\frac{\partial}{\partial\theta_x}\langle m|\frac{\partial}{\partial\theta_y}|m\rangle - \frac{\partial}{\partial\theta_y}\langle m|\frac{\partial}{\partial\theta_x}|m\rangle\right) \tag{7}$$

is the Hall conductivity of the mth eigenstate with energy E_m and Θ is the Heaviside step function [11, 12, 10]. Then, it has been shown that the boundary condition averaged Hall conductance for a state m is:

$$\langle\delta\sigma_{xy}(m)\rangle = \frac{e^2}{h}C(m) \tag{8}$$

where $C(m)$ is the Chern number for the given state. The Chern number is necessarily an integer-valued topological invariant characterizing the wavefunction [10, 6]. As mentioned in Sec. 1, the Chern number thus directly measures the capacity of an eigenstate to carry Hall current and is therefore a measure of its extensiveness. States with $C \neq 0$ are extended, and have wavefunctions which can be made to vanish at any given position in space, while states with $C = 0$ are localized and have nodes that are confined in space. The total sum of Chern numbers for all states in a given LLL system must be one [6, 13].

A robust methodology for computing Chern number is presented in [20] and is sometimes referred to as the Fukui-Hatsugai-Suzuki method. The boundary condition space $\vec{\theta} = (\theta_x, \theta_y)$ is discretized into a $2\pi \times 2\pi$ grid. This grid is comprised of $N_\theta \times N_\theta$ points where N_θ is a computational parameter that defines the resolution of the grid as $\Delta\theta = \frac{2\pi}{N_\theta - 1}$. It is important to note that due to the periodicity in twist angle θ, values of 0 or 2π are equivalent. However, allowing the grid to wrap around to both values allows for simplicity in subsequent calculations without significantly impacting the efficiency. One can consider this setup as a toroidal mesh that is formed by joining opposing segments of the θ grid such that points at 0 and 2π are affixed.

For this grid, two primitive vectors in the x and y directions may be defined, $\hat{x}$ and $\hat{y}$, with length $\Delta\theta$. Then, a $U(1)$ link variable may be defined for the mth eigenstate $|\psi_m(\vec{\theta})$,

$$U_\mu^m(\vec{\theta}) = \frac{\langle\psi_m(\vec{\theta})|\psi_m(\vec{\theta}+\hat{\mu})\rangle}{|\langle\psi_m(\vec{\theta})|\psi_m(\vec{\theta}+\hat{\mu})\rangle|} \tag{9}$$

where $\mu = x, y$ and the denominator is effectively a normalization factor. The Berry phase at a unit cell at $\vec{\theta}$ may be calculated by the gauge invariant formula:

$$\gamma_m(\vec{\theta}) = \frac{1}{i}\log\left(\frac{U_x^m(\vec{\theta})U_y^m(\vec{\theta}+\hat{x})}{U_x^m(\vec{\theta}+\hat{y})U_y^m(\vec{\theta})}\right). \tag{10}$$

For sufficiently fine discretization, these local Berry phases may be restricted to $(-\pi, \pi]$ during numerical computation. The Chern number of a given eigenstate is finally given as the sum over the discretized Berry phase contributions:

$$C(m) = \frac{1}{2\pi}\sum_{\vec{\theta}}\gamma_m(\vec{\theta}). \tag{11}$$

This method yields Chern numbers that are strictly integer-valued [20].

3 Methods

Simulations for this system are implemented such that a large quantity of data may be collected to analyze the ensemble-averaged system properties. One iteration or trial of data-collection consists of the following steps:

1. Initialize a random potential $V(\mathbf{r})$
2. Solve for the eigenvectors and eigenvalues of the Hamiltonian over a grid of $\vec{\theta}$
3. Compute Chern numbers for all states
4. Save data

The entire simulation is implemented in Python, heavily relying on the NumPy mathematical library for computations. Since the entire process is computationally expensive, considerable efforts have been made to optimize the simulation pipeline through profiling and timing the code. Where possible, operations are vectorized and parallelized to fully utilize the available computational resources. The Python library Numba is used for CPU optimizations and the library CuPy is used to offload certain computations to GPU. All computations are performed with double-precision complex numbers: both the real and imaginary parts are stored with 64-bit precision, corresponding to approximately 16 decimal places of precision [21]. In total, computations are performed for 145,539.09 CPU hours and 4,277.02 GPU hours across Princeton's Della and Adroit research computing clusters. A variety of CPU-types are used for simulations and NVIDIA A100 GPUs are used for simulations with large system sizes. For reference, these timing metrics would translate to over 47 days of non-stop computing with 128 CPU cores and about 45 days of non-stop computing with $4\times$ NVIDIA A100 GPUs. The simulations amount to a total of 69.54 GB of data collected. As system sizes increase, simulations also begin to utilize a very large amount of memory to store eigenvalues and eigenvectors across the boundary condition grid. As such, memory usage per-trial is limited to around 200GB for CPU-only trials and about 80GB for CPU-GPU trials. A dynamic approach is implemented to reduce the amount of re-computation required from the limited memory by carefully traversing the boundary condition grid and releasing data from memory when its no longer needed. The entire simulation code-base has been made available publicly on GitHub at: `github.com/edeleu/iqhe-simulation`.

For each trial, the program records the energy eigenvalues for four boundary conditions: $\vec{\theta} = (0,0), (0,\pi), (\pi,0), (\pi,\pi)$, the Chern numbers of all states, and the random potential realization for repeatability. Since the random potential realizations are saved, the eigenvalues or eigenvectors at arbitrary boundary conditions may be computed for later analysis if required. Data is collected for system sizes between $N_\phi = 8$ and $N_\phi = 2048$ states. At this time, collecting a large scale dataset for larger systems is infeasible with the given approach. Collecting one trial of data for $N_\phi = 2048$ states takes approximately 100 minutes using high-end hardware. To increase the effective rate of data-collection, a large number of trials are run simultaneously. Resources are primarily allocated for data-collection of large system sizes, since the characteristics of their eigenvalue spectra are of particular interest. The subsequent sections explain in detail the constituent components of the

simulation pipeline.

3.1 Random Potential

For simplicity, the two-dimensional Gaussian white-noise potential is initialized in Fourier-space for direct compatibility with Equation 5. In practice, constructing a real-space potential and subsequently extracting Fourier coefficients takes considerably more time using a fast Fourier transform (FFT) algorithm. The random potential is represented as a finite-valued, discrete Fourier-space grid. A $(2M+1) \times (2M+1)$ grid is initialized such that the center position of the zero-indexed grid, $V[M, M]$, represents the $V_{0,0}$ zero-frequency (DC) Fourier coefficient. The value of M is chosen to scale with $4\sqrt{N_\phi}$ such that the potential grid is sufficiently large for a given number of states and the microscopic grid spacing $a_o = L/M$ is small compared to the magnetic length ℓ_B [19]. This setup allows for straightforward indexing: four quadrants naturally arise in the grid, corresponding to positive and negative values of the Fourier indices. For simplicity, the zero-frequency coefficient is set to zero to ensure no offset with the real-space potential, enforcing $\langle V(\mathbf{r})\rangle = 0$. Then, real and imaginary parts of the coefficients $V_{\mathbf{q}}$ are independently sampled from an $\mathcal{N}(0,1)$ normal distribution in the regions of $0 \leq q_1 \leq \pi/a_o$ and $-\pi/a_o \leq q_2 \leq \pi/a_o$, corresponding to the two quadrants of the grid with positive q_1 and positive or negative q_2. Since the real-space potential must be entirely real-valued, the constraint $V^*_{\mathbf{q}} = V_{-\mathbf{q}}$ is imposed and used to set the remaining two quadrants of Fourier coefficients in the grid. Finally, the coefficients themselves must be scaled before computation in the Hamiltonian. Since the overall number of Fourier coefficients in the matrix grows with $\sim N_\phi$, the variance of the real-space potential will also grow. The variance may be given by $\langle (V(\mathbf{r}) - \langle V(\mathbf{r})\rangle)^2\rangle$, but since $\langle V(\mathbf{r})\rangle = 0$ for the Gaussian white noise potential, the variance is simply $\langle V(\mathbf{r})^2\rangle$. Thus, the entire matrix is divided by $\sqrt{N_\phi}$ to ensure constant variance of the random potentials and a consistent eigenvalue range between all system sizes.

Using FFT functionality with the SciPy Python package, it is simple to transform the grid of Fourier coefficients into the corresponding real-space random potential. Fig. 1a depicts a visualization of one such random potential as a 2D map where the color corresponds to the magnitude of the potential. Fig. 1b visualizes the same random potential in 3D space. Visually, the potential appears as expected: the potential has zero-mean, random amplitudes at random locations, and no obvious

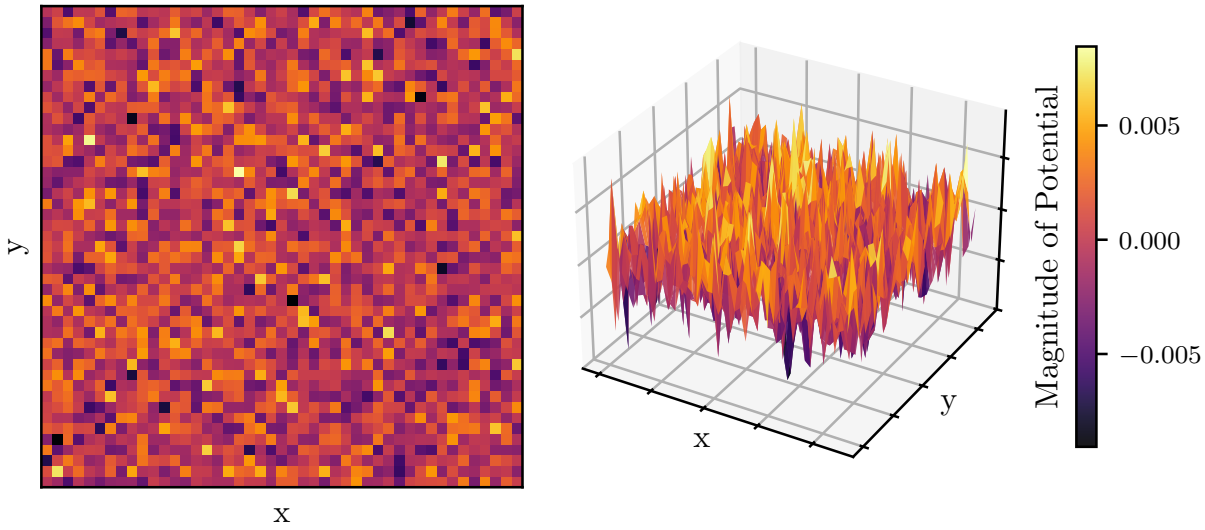

Figure 1: Visualization of a random potential corresponding to an $N_\phi = 64$ square sample in real-space. (A) Color-coded 2D projection of the random potential. (B) 3D representation of the random potential where the height represents potential magnitude.

spatial correlations. In practice, the potential generation step takes negligible time, as a result of the efficient Fourier-space construction.

3.2 Hamiltonian Computations

The most crucial step in the simulation process is the construction and subsequent diagonalization of the Hamiltonian to compute the energy eigenvalues and eigenvectors for a given set of boundary condition twist angles. The Hamiltonian is first constructed according to Equation 5 in an optimized and parallelized manner to speed-up the summation operation. Each exponential term is pre-computed and stored in a look-up-table to minimize repetitive, time-consuming exponential computations and replace them with faster matrix retrieval operations. For example, each pre-computation table is indexed with two of the variables to maintain reasonably sized look-up-tables and, in practice, the fastest data retrieval. There are look-up-tables for $(m, n), (m, \theta_y), (m, j)$. As a consequence of the negative exponent in $e^{-i\frac{n\theta_x}{N_\phi}}$ and otherwise identical exponential form to $e^{i\frac{m\theta_y}{N_\phi}}$, an (n, θ_x) table is not required since the (m, θ_y) table may be used with division of the pre-computed term rather than using multiplication. Hamiltonian values are only computed for the lower triangular section of the matrix: the upper triangular section is not required since the

matrix is Hermitian and a lower triangular matrix is sufficient for the subsequent diagonalization algorithm.

With the given optimizations, the Hamiltonian construction takes minimal time compared with its diagonalization which is by far the most time-consuming operation in the simulation pipeline. This is accomplished with the NumPy library's highly-optimized linear algebra capabilities. Systems below $N_\phi = 512$ states are simulated utilizing CPU-only systems. However, the Hamiltonian matrix has size $N_\phi \times N_\phi$, and hence, the diagonalization process becomes extremely slow for large systems with worst-case time complexity of $\mathcal{O}(N_\phi^3)$ [22]. The CuPy library is used to diagonalize matrices using GPUs for systems of $N_\phi = 512$ and above, yielding a speedup of $2 - 5\times$ compared to the CPU only simulations.

The Hamiltonian must then be solved repeatedly for an entire boundary condition grid for subsequent Chern calculations. The eigenvalues and corresponding eigenvectors from the diagonalization algorithm are always returned in increasing order. According to the adiabatic theorem, if the parameters of a Hamiltonian are varied sufficiently slowly, a system initially in a given non-degenerate eigenstate will remain in the same instantaneous eigenstate without excitation to higher or lower states, provided there are no level crossings between states [23, 1]. In this work, it is assumed that the eigenstates at different boundary conditions correspond to one another without any level-crossings, an assumption justified with the presence of disorder [23, 1]. This assumption forms the the basis for the Fukui-Hatsugai-Suzuki method of Chern number computation [20]. Fig. 2 depicts the energy surfaces across a $2\pi \times 2\pi$ boundary condition grid for various random potential realizations in an $N_\phi = 8$ system. This demonstrates the various ways in which the eigenvalue surfaces may warp as the twist-angles are varied. Furthermore, these surfaces may get arbitrarily close to one another, but crossings and intersections never occur. Preliminarily, this ensures the validity of the computations and simulation set-up.

3.3 Chern Number Computation

In practice, the Chern computation given in Sec. 2 may be simplified given a few fundamental principles. First note that for a complex number, $z = a + bi = re^{i\theta}$ where $r = |z|$ and θ is the phase

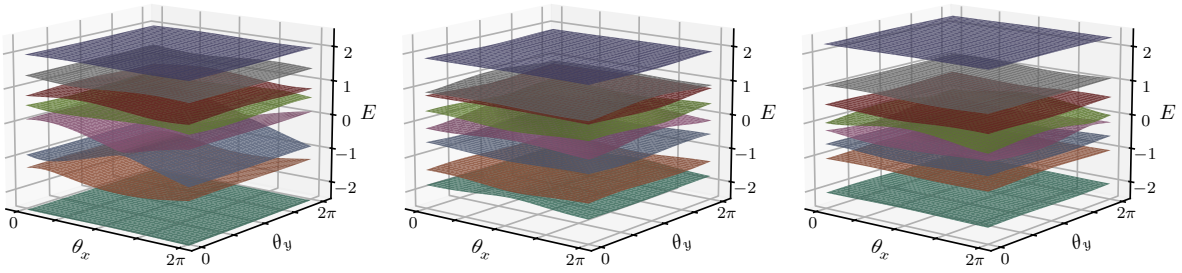

Figure 2: Energy surfaces for an $N_\phi = 8$ system simulated over a grid of θ_x and θ_y. Results for three different random potentials are displayed, illustrating variations in the energy landscapes across the parameter space.

angle. Then, the complex logarithm may be broken down as $\log(z) = \ln(r) + i\theta$. The defined link variable in Equation 9 is always normalized to have a magnitude of one due to the normalization factor in the denominator. The entire argument of Equation 10 for the Berry phase at a unit cell $\vec{\theta}$ thereby has magnitude of unity since multiplying and dividing by magnitude-one variables only changes the phase. Thus, this logarithm effectively simplifies to $i\theta$ since $\ln(1) = 0$. With the leading factor of $1/i$, the Berry phase is simply the angle θ of the argument contained within the logarithm. For efficient computation, the normalization in the denominator of Equation 9 is not necessary. Finally, consider that for complex inner products, $\langle a|b\rangle^* = \langle b|a\rangle$. Then, the order of the inner products may be flipped for the terms in the denominator of Equation 10 to yield the negative contribution to the given Berry phase angle. Putting this all together, the simplified formula for the Berry phase of a given unit cell at $\vec{\theta}$ is:

$$\gamma_m(\vec{\theta}) = \arg\Big(\langle\phi_m(\vec{\theta})|\phi_m(\vec{\theta}+\hat{x})\rangle \cdot \langle\phi_m(\vec{\theta}+\hat{x})|\phi_m(\vec{\theta}+\hat{x}+\hat{y})\rangle \cdot \langle\phi_m(\vec{\theta}+\hat{x}+\hat{y})|\phi_m(\vec{\theta}+\hat{y})\rangle \cdot \langle\phi_m(\vec{\theta}+\hat{y})|\phi_m(\vec{\theta})\rangle\Big). \quad (12)$$

Conveniently, the $\arg()$ function has a simple implementation in Python with NumPy and is restricted to the range $(-\pi, \pi]$. While this expression is lengthy, it greatly simplifies the Chern number computation and allows for major speed-ups through vectorized operations to simultaneously compute the Chern numbers for all states. This expression also gives an insight into the Chern computation itself: the Berry phase computation effectively traverses each $\vec{\theta}$ unit cell counterclockwise to find its local phase. These phase contributions are then summed over all cells to

find the Chern number.

3.4 Chern Number Convergence

The number of grid-points N_θ in the $2\pi \times 2\pi$ θ-space is an important system size dependent parameter that must be fine-tuned to ensure accurate Chern number computation. The main source of error in Chern number computations will result from inadequate discretization of the boundary condition grid [13]. One quick method to determine if the Chern numbers for a given trial are correct is to check that their sum is one. A previous work [13] estimates the error rate for each Chern number computation from sign errors in local Berry phases, then choosing a grid resolution that is sufficiently large to ensure a low trial rejection rate.

While this method seems sufficient, further analysis of grid resolutions has demonstrated a more complex landscape. While Chern numbers may correctly sum to one for a given grid resolution, this does not ensure that the Chern numbers for a sample have are accurate and have converged to their true values. Oftentimes, only a quite low number of grid points N_θ is needed to yield trials where the Chern numbers sum to one with a low rejection rate far below 0.1%. However, incrementally increasing the number of grid points has shown that Chern numbers for a given system may actually flip once a certain resolution is reached. Up to this resolution, the results may be completely stable, giving a deceiving appearance of correctness. Subsequently improving the resolution may either result in more flipping of states such that they return to the original values, or stabilizing at new values. This demonstrates that the smaller grids are not adequately capturing the topological properties, and flipping occurs once features are properly captured by a finer grid spacing. The instability from subsequently finer grids may result from moving away from the exact twist angles that were required for stabilization.

Thus, an insufficient grid resolution will not properly capture the energy landscape and topological properties of a system to ensure accurate Chern numbers. When Chern numbers are found to be unstable due to the grid resolution, one of only several scenarios are observed (or their reverse):

- Consecutive Chern-0 states transform to $(C = 1, C = -1)$
- Consecutive states $(C = 0, C = \pm 1)$ switch order to $(C = \pm 1, C = 0)$

- Consecutive states $(C = 1, C = -1)$ transform to $(C = 1, C = 0, C = -1)$ or similar combinations where a Chern-0 state forms or is annihilated

In most of the situations where flipping and instability occurs, the sum of Chern numbers deceivingly remains at one. Typically, this corresponds to the energy-surfaces of consecutive states becoming extremely close to one-another or beginning to touch. However, looking at the closest distance between eigenvalues in boundary condition space does not reliably predict when the computation requires an improved grid resolution.

In an ideal scenario with infinite computing power, N_θ could be set to an arbitrarily large value to ensure 100% accurate Chern numbers. However, the Hamiltonian must be solved for each (θ_x, θ_y) in the boundary condition grid. The runtime for a trial is thus proportional to the number of grid points. Since the process of diagonalizing the Hamiltonian is already time-consuming, especially for large systems, it is desirable to minimize the size of the θ-grid while maintaining an acceptable precision. An algorithm was developed to collect data specifically for Chern number convergence. This program begins by computing Chern numbers for a high number of grid-points N_θ between 60 and 120 depending on system size. This is the "reference" solution, relying on the fact that a sufficiently fine grid will capture all the features of the system and yield correct Chern numbers. If the solution does not have Chern states summing to one, an even higher resolution is attempted, although this is rarely observed. The program then iteratively solves the Hamiltonian and computes Chern numbers for the same random potential with N_θ increasing from a minimum specified value such as 10. Once there are 5-consecutive grid resolutions that all have consistent Chern numbers that match the "reference" values from the higher precision grid, the trial is recorded. The smallest N_θ in the window of 5 is used as the converged resolution. While this method is still imperfect, it helps to better understand the reliability of the results and achieve more accurate Chern numbers. This program is run for system sizes up to $N_\phi = 512$, although smaller system sizes have considerably more data since the systems are faster to simulate. This convergence data is then plotted in Fig. 3, where the solid black line represents the number of grid points N_θ where 99% of trials have achieved Chern number convergence. A power-law fit is performed, in dotted red, so that the 99% grid resolution may be forecasted up to larger system sizes where it is infeasible to collect convergence data for a statistically relevant number of trials. The experimental data agrees

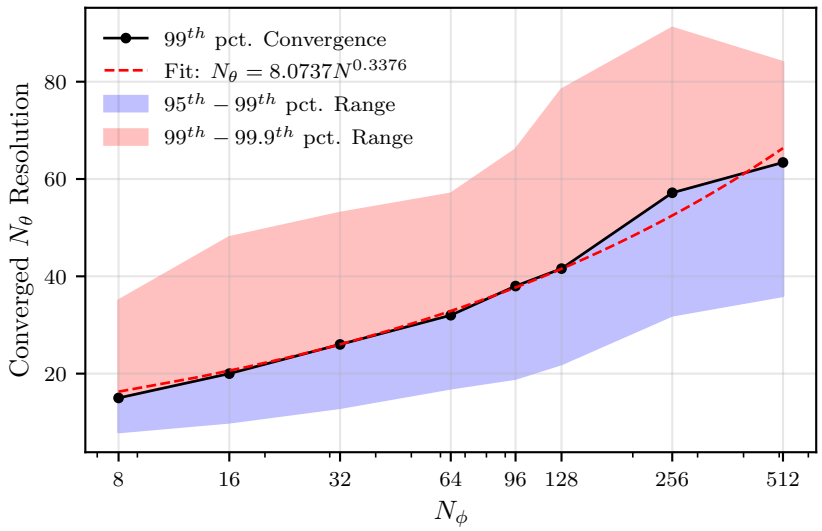

Figure 3: Converged N_θ Resolution vs. System Size N_ϕ (log-axis). The 99th percentile convergence (black line) is fit by $N_\theta = 8.0737N_\phi^{0.3376}$ (dashed red). Shaded regions show the 95th–99th (blue) and 99th–99.9th (red) percentile ranges.

quite well with this fit, although some deviations are seen for the larger system sizes with less data. This yields the fit $N_\theta = 8.0737N_\phi^{0.3376}$ with $R^2 = 0.98$, demonstrating the expected relationship that larger systems require finer grids. Considering that the boundary condition grid has N_θ^2 total points, the number of Hamiltonian matrices that must be solved thus scales with $N_\phi^{0.6752}$. Combining this with the scaling of the diagonalization process, this yields a worst-case time complexity of $\mathcal{O}(N_\phi^{3.68})$ which is far from ideal. However, the actual runtime often scales less significantly due to the highly-optimized hardware for large matrix computations.

Because large-scale data collection is quite fast for lower system sizes, the 99.9% resolutions are used for data collection in systems up to $N_\phi = 512$. For larger systems, the forecasted 99% convergence resolutions are used. It follows that according to these estimates, 99.9% of the data collected for systems up to $N_\phi = 512$ should have correct, converged Chern numbers. For larger systems, the reliability should be around 99%.

4 Chern State Characterization

Table 1: Chern Number Distribution Statistics

	# of	# of Values for $C =$							$\% \, C \neq 0$	Total #
N_ϕ	Trials	-3	-2	-1	0	1	2	3	Eigenvalues	Eigenvalues
8	528,881	1	99	131,917	3,438,475	660,118	439	0	18.732%	4,231,049
16	191,478	0	126	134,780	2,602,522	325,925	294	0	15.052%	3,063,647
32	521,472	0	1054	817,295	14,529,581	1,337,474	1699	1	12.929%	16,687,104
64	96,957	1	427	300,730	5,506,145	397,346	599	0	11.266%	6,205,248
96	51,804	0	411	232,771	4,455,090	284,427	485	0	10.418%	4,973,184
128	12,744	0	145	73,937	1,470,344	86,641	165	0	9.863%	1,631,232
192	17,837	0	262	146,249	3,113,904	163,968	321	0	9.075%	3,424,704
256	6601	0	158	68,576	1,545,790	75,171	161	0	8.525%	1,689,856
512	8105	1	337	149,548	3,841,923	157,578	373	0	7.418%	4,149,760
1024	21,222	3	1931	689,985	20,326,314	711,112	1983	0	6.465%	21,731,328
2048	6942	1	1219	393,564	13,420,663	400,592	1176	1	5.603%	14,217,216

A summary of the data collected for each system size, including the distribution of Chern-states, is presented in Table 1. Data collection is primarily performed for systems $N_\phi = 1024$ and $N_\phi = 2048$ since these will have the most informative energy separation statistics. Several million eigenvalues are also collected for the other displayed system sizes for completeness. This requires small systems such as $N_\phi = 8$ to have a massive quantity of trials, above $500{,}000$, while larger systems such as $N_\phi = 512$ have significantly fewer trials. The fluctuations in amount of data collected per system size result from differences in computing performance and allocated simulation run-times. The data demonstrates that the fraction of non-zero Chern states decreases as system size increases. As expected, a majority of eigenvalues are $C = 0$ localized states. A majority of $C \neq 0$ data has $C = \pm 1$: there is a slight bias towards $C = +1$ states, differing by approximately the number of trials for each system size– this is logical, since the sum of Chern numbers must always sum to one for a given trial. There is a minimal amount of data with $|C| > 1$, despite the significant number of trials simulated. For large system sizes, the rate of $C = -2$ and $C = 2$ states are quite consistent, although smaller systems are biased toward $C = +2$. For $N_\phi = 2048$, the rate of states with $C = \pm 2$ is approximately 1 in 5,936 states; thus, there should be at least one of these states in every three trials simulated. However, for $C = \pm 3$ with $N_\phi = 2048$, the occurrence is only 1 in 7,108,608 states. Across all of the data collected, there are no states with $|C| > 3$.

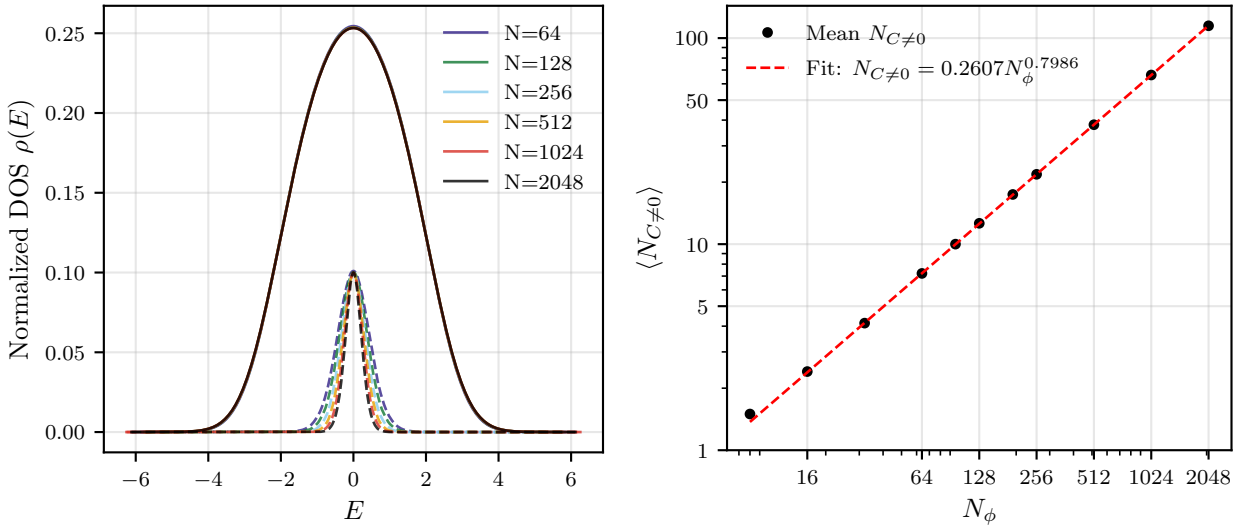

Figure 4: (A) Normalized Density of States $\rho(E)$ vs. Energy E for all eigenvalues (solid lines) and for nonzero Chern eigenvalues (dashed lines), plotted for systems of various sizes. (B) Log-log plot of ensemble averaged number of nonzero Chern states $\langle N_{C\neq0}\rangle$ vs. System Size N_ϕ.

For this, and subsequent sections, the data ensembles are effectively symmetrized by adding "virtual" trials that mirror the eigenvalue spectra compared to the collected trials. For example, a fictitious trial with eigenvalues $[-2.3, -1.1, 0, 1, 2.5]$ would yield a new "virtual" trial with eigenvalues $[-2.5, -1, 0, 1.1, 2.3]$. This symmetrization procedure allows for more robust statistical analysis by effectively doubling the amount of data, and it is justified by the electron-hole symmetry of the random potentials.

Normalized density of states (DOS) histograms are then plotted for an assortment of system sizes, such that the area under the curves are normalized to unity. The eigenvalues for this section, and the remainder of the report, are chosen for the $\vec{\theta} = (\pi, \pi)$ boundary conditions. This is an arbitrary choice, and any other boundary condition should yield the same statistics for the ensemble of data. A Gaussian kernel-density-estimation (KDE) algorithm is applied to yield smooth DOS curves: this method estimates a continuous probability distribution from finite data using a sum of Gaussian kernels [24]. The kernel bandwidth is taken to be sufficiently small as to capture all the details of the probability distributions without over-smoothing the data. This is depicted in Fig. 4a: the solid curves represent the overall DOS for all eigenvalues and the dashed curves represent the DOS for all $C \neq 0$ extended states. For all system sizes plotted, the overall DOS curves almost completely overlap over the entire eigenvalue spectrum, yielding one darkly colored curve. There

appears to be some slight deviation at the peak of the DOS at the center of the band with the $N_\phi = 64$ system. This is likely an artifact of the fitting methodology rather than the underlying distribution itself. The plot also presents dashed DOS curves for the $C \neq 0$ states which have total area corresponding to the fraction of $C \neq 0$ eigenvalues from Table 1. These curves are neatly localized around zero at the center of the band. As the system sizes increase, the width of the curves decrease and the extended states cluster more closely around $E = 0$. In the thermodynamic limit of $N_\phi \to \infty$, this supports the conclusion that the extended states will be confined at the band-center $E = 0$, supporting the results of previously conducted studies [19, 13]. The peaks of these dashed DOS curves are also relatively consistent, demonstrating that the fraction of extended states at $E = 0$ in the thermodynamic limit will be finite. Experimentally, this fraction of extended states at $E = 0$ is somewhere between 39% and 40%, although the exact proportion varies based on the fitting methodology.

The scaling behavior of the extended states is now studied more concretely. For each trial, the number of $C \neq 0$ states is tabulated, averaged for each system size, and subsequently plotted in a log-log plot in Fig. 4b. The error-bars are negligible compared to the size of the plotted points. The standard errors are then used to weight the data points in a fitting procedure, yielding the fit $N_{C\neq 0} = 0.2607 N_\phi^{0.7986}$. The data for $N_\phi = 8$ is excluded from this fit, since this system requires finite-size corrections as discussed in [25, 13]. The very small system sizes may be expected to deviate from the behavior of larger systems: this deviation results from the relatively small areas in the smaller systems, whereby the wavefunctions may have considerable size that is extended over the sample edges with the periodic boundary conditions. This differs from larger systems which have sufficient area such that the periodic behavior at the edges is negligible. Small-systems aside, there is an extremely robust fit for the pre-factor and exponent with $R^2 = 1.0$. Theoretically speaking, the extended states scale with $N_{C\neq 0} \sim N_\phi^{1-\frac{1}{2\nu}}$ [13]. Re-fitting to this functional form yields the localization length exponent $\nu = 2.4830 \pm 0.0035$ which agrees precisely with the value of $\nu = 2.48$ reported in [13], confirming the validity of the simulated data. This consistency may be expected as similar experimental procedures and Hamiltonian construction are employed. Still, the precise value of the localization length exponent ν depends on the exact methodologies followed and is not universally agreed upon; older studies reported values around $\nu \approx 2.3 - 2.4$ [10, 26], while more modern studies have found higher values ranging from $\nu = 2.48$ to $\nu = 2.61$ [27, 13].

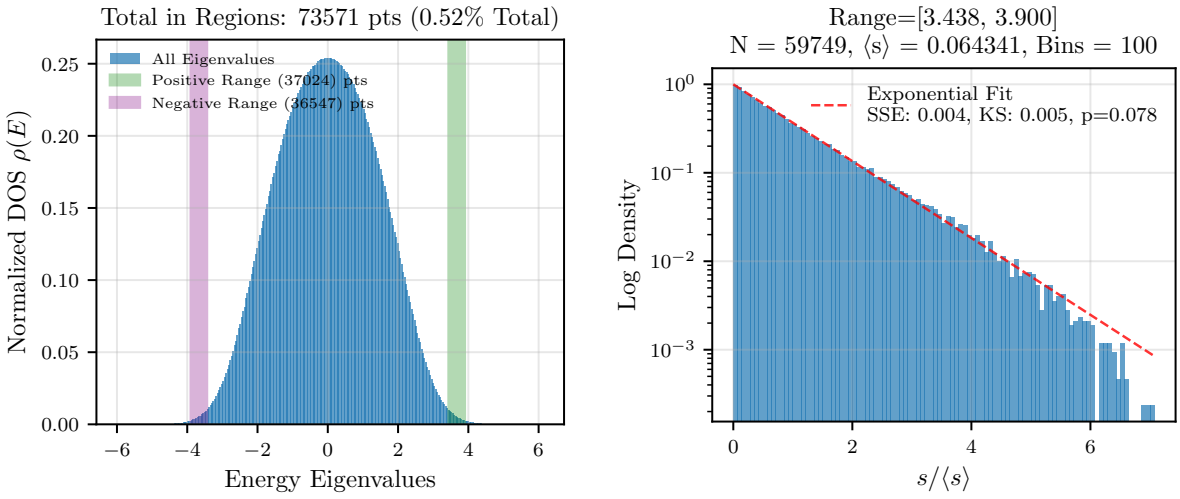

Figure 5: (A) Normalized density of states $\rho(E)$ for a system of size $N_\phi = 2048$, with two symmetric energy windows (green and magenta) highlighted. (B) Logarithmic density of normalized level spacings $s/\langle s\rangle$ for eigenvalues within the highlighted energy windows. The red dashed line shows an exponential fit $P(s) = e^{-s/\langle s\rangle}$, characteristic of Poisson statistics.

5 Level Spacing Statistics

The distributions of eigenvalue separations $s_i = E_i - E_{i-1}$, known as level spacings, are now studied for various scenarios. These are studied for the $N_\phi = 2048$ system since these trials have the most eigenvalues and should yield the most robust separation statistics. The data is not symmetrized in this section, but this step is not strictly necessary and has no impact on the resulting distributions since they are constructed in a symmetric manner and density plots are all normalized to have constant area. For the subsequent plots, the level spacings are normalized by the ensemble-average $\langle s\rangle$ computed individually for each set of separations. This allows for comparison to the theoretical Poisson and GUE distributions which assume normalized data [16].

The edges of the LLL have limited density of states. In the tails of the eigenvalue distributions presented in Fig. 4, it is highly unlikely for an extended state to be present in this region. In practice, only Chern-0 and hence localized states are present. These states should follow Poisson statistics since they are tightly localized in space and should have no level repulsions. In the tails of the eigenvalue distribution, a small window of eigenvalues is analyzed, with windows in both the positive and negative regions of the eigenvalue spectrum for symmetry. The window-size is chosen

to be as narrow as possible, near the edges of the distribution, while still containing a sufficient number of eigenvalues to analyze separation data with 5 to 10 separations per trial. An algorithm is developed to find the ideal window-size for these constraints by iteratively computing the distributions and narrowing the windows. The selected windows of eigenvalues and the corresponding separation histogram are displayed in Fig. 5. These regions together contain $73{,}571$ eigenvalues, corresponding to 0.52% of the total $N_\phi = 2048$ dataset with $59{,}749$ separation data points. This logarithmic histogram plot displays how the eigenvalues in these edge regions very neatly follow Poisson statistics with the fit $P(s) = e^{-s/\langle s\rangle}$. A Kolmogorov–Smirnov test is performed to ensure the validity of the fit: the test yields a p-value of 0.078, which is above the standard threshold of $p = 0.05$. This indicates that there is no statistically significant evidence to reject the null hypothesis (i.e., the distributions are the same), and so, the observed separation data is consistent with being drawn from a Poisson distribution. The data slightly falls-off above $s/\langle s\rangle$, but this can be attributed to the finite window size where only a maximum value of $s/\langle s\rangle = 7.18$ is possible with the given mean separation. Notably, there is significant density at $s = 0$, indicating that these states experience no level repulsion and may be arbitrarily close to one another. Further analysis of these localized states and their distributions is presented in Appendix A for other system sizes and window-sizes.

The level spacing data for the Chern-0 states is relatively straightforward near the band edges. Now, the data at the center of the eigenvalue spectrum will be analyzed for various Chern configurations: all Chern, $C \neq 0$, $C = 0$ or $C = 1$, $C = +1$, and $|C| = 1$. The $C = -1$ data is not depicted, although it is experimentally verified to be the same as the $C = +1$ scenario. For each trial, the eigenvalues are first confined to the given window size and the eigenvalues are then filtered to match the corresponding Chern configuration. The separations may then be computed and the ensemble-average separation may be found for each given set of data for normalization. The window size at the center of the band is minimized such that there are still a reasonable amount of separation values for all of the Chern filters. This data remains unfitted, but it is still reasonable to draw conclusions about the trends and characteristics of the different types of states by overlaying different distributions. As a consequence of the construction method, the level spacings for Chern configurations other than all Chern may consider non-consecutive states. For example, consider a series of states of Chern character $[0, 0, 0, -1, 1, 0, 0, 1]$. If the Chern filter is $|C| = 1$, the level

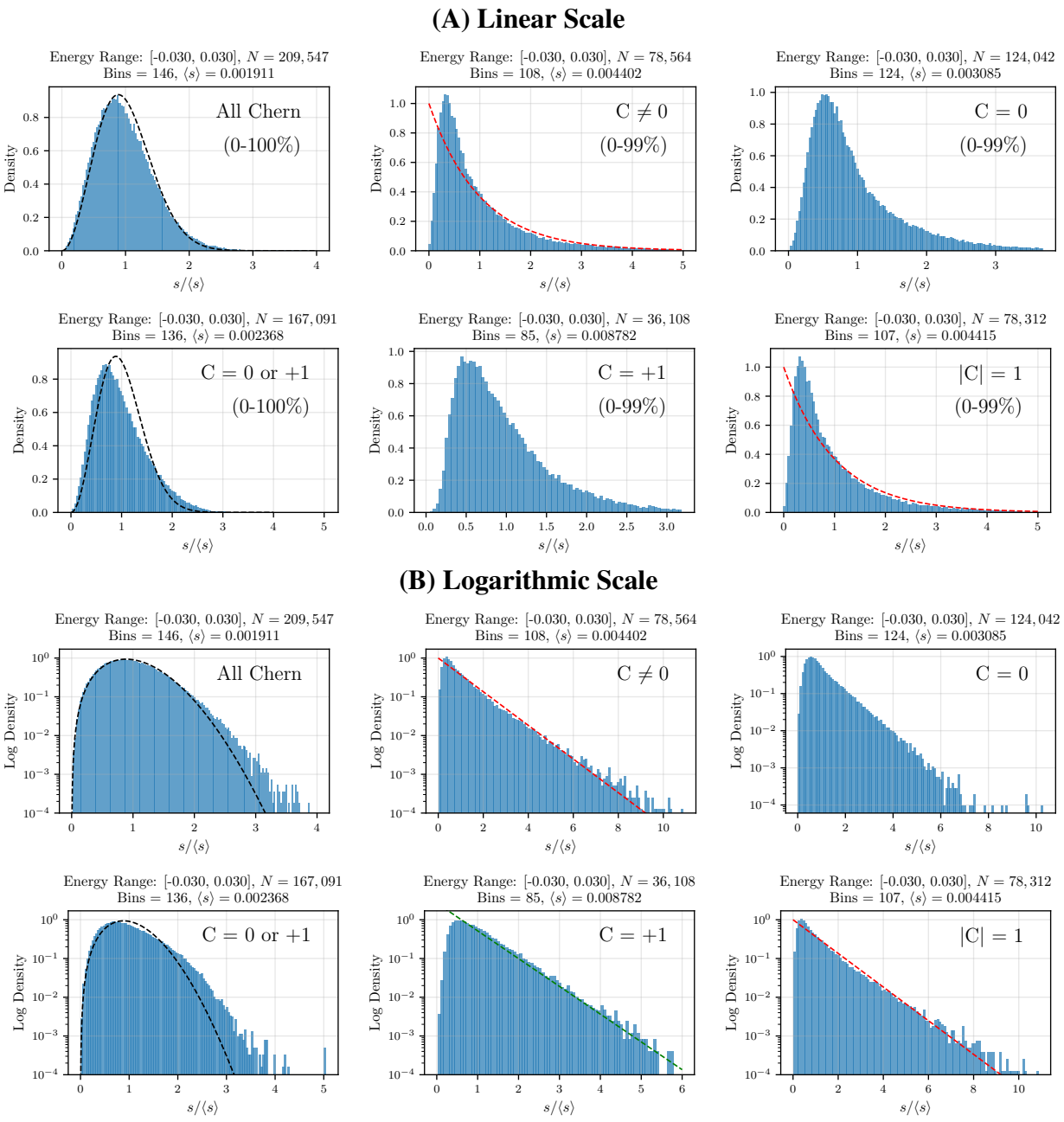

Figure 6: Normalized level spacing $s/\langle s \rangle$ distributions for eigenvalues within the central energy window $[-0.03, 0.03]$ for a system of size $N_\phi = 2048$. Each panel shows results filtered by Chern number, with the total number of level spacings N, bin count, and mean spacing $\langle s \rangle$ indicated above each plot. Overlaid black dashed curves indicate the GUE probability distribution; red and green dashed curves indicate various Poisson distributions. (A) Linear-scale histograms. Annotations indicate the percentile range of spacings included in each histogram (e.g., 0–99%). (B) Corresponding log-scale representations, highlighting differences in tail behavior.

spacings will then be computed between the $-1, 1$ states and the $1, 1$ states in the given scenario, skipping over the Chern-0 states.

Fig. 6 presents this data on both linear and semi-logarithmic y-axis plots. For the linear plots, the annotated percent ranges indicate the cutoff of the x-axis: for visual clarity, some plots are cut off at the 99th percentile as a consequence of the data having very long tails. The GUE Wigner surmise is overlaid on the all Chern plots with a dashed black curve. This all Chern configuration considers the level spacings between all consecutive states, irrespective of Chern character. The all Chern plots demonstrate that the probability density at the center of the LLL is close to following GUE statistics with deviation in the tail behavior. One would expect GUE statistics in this region since there is the highest density of extended states and there should be significant level repulsions. The fit is quite good up until $s/\langle s\rangle = 2$, after which the GUE prediction quickly drops off and deviates from the observed data. The experimental data depicts more significant density in the tail and appears to remain linear on the logarithmic density plot. This indicates that states most closely separated near $E = 0$ certainly follow GUE statistics, while states further apart actually approach Poisson statistics with a tail approaching the form of $\sim e^{-s}$ rather than $\sim e^{-s^2}$ as the GUE would predict. This likely results from the relatively high proportion of localized states, even in this narrow window size. Localized states separating extended states may result in the dominating Poisson-like behavior in the tail. With a further decrease in window size, the Poisson contribution likely decreases and the overall distribution would likely more closely match the GUE statistics.

Next, it is informative to study the separation statistics between states of certain Chern character. The eigenvalues are next filtered to states with $C = 0$ or $C = 1$, and the level spacings are computed. The level spacings are a combination of Chern-0 spacings as well as mixed $[0, 1]$ separations. While the density plots for the $C = 0$ or $C = 1$ case look similar to the all Chern scenario, the GUE fit is quite poor with a misaligned and flattened peak. This may be expected since the $C = -1$ states are not considered, removing about half of the extended states and increasing the average separation for this configuration compared to the all Chern scenario. The tail of the plot appears to fall off quicker than linearly on the logarithmic density plot, although still not as fast as the GUE curve. There should be limited repulsion between consecutive extended and localized states due to limited wavefunction overlap. This scenario represents the beginning of a

transition from the GUE statistics of the all Chern scenario to more Poisson-like statistics of the localized states. Although there is high density of $C = 1$ states in this window, there will be a much higher proportion of localized states. The level repulsions between extended states dominate this distribution, even though only $C = 1$ extended states are strictly considered.

The plots for the $C \neq 0$ and $|C| = 1$ configurations are almost identical. This is expected considering there are very few states with $|C| > 1$, as affirmed by the difference of 252 separation data points between the two plots. The following discussion is hence targeted toward the all extended state $C \neq 0$ scenario. The Poisson distribution $P(s) = e^{-s/\langle s \rangle}$ is depicted with dashed-red lines on these plots; the data appears very Poisson-like, although with deviation and a slight "nose" near zero. The linear plot indicates that the data is not quite an exponential distribution in the neighborhood of zero, with limited density. The density ramps up from zero to the peak density of one, affirming that extended states in this region experience level repulsion preventing them from being arbitrarily close to one another. Beyond slight separations, the extended states appear to follow Poisson-like statistics with nearly exponentially distributed separations. The average separations for this extended state configuration are approximately twice those of the all Chern scenario. This indicates that within this window, the extended states are often separated by at least one localized state. This may explain the Poisson-like behavior for the bulk of the distribution: the statistics for localized states interspersed between extended states may dominate, limiting the repulsive effects between non-consecutive extended states.

The level spacings between similar Chern character, $C = +1$ states, will now be analyzed. This situation ignores level spacings between different types of extended states as in the $C \neq 0$ case. Near zero, the separation density between $C = +1$ states increases with upwards concavity in the linear plot, potentially demonstrating some level repulsion between $C = +1$ states. However, it is also likely that this results from interspersed $C = 0$ or $C = -1$ states causing larger separations between $C = +1$ states. The average separation $\langle s \rangle$ between $C = +1$ states is considerably larger than the other scenarios and is another $2\times$ larger than the $C \neq 0$ case, indicating that it is unlikely to find consecutive $C = +1$ extended states. While the bulk of the distribution appears Poisson-like in the logarithmic plot, the scale is quite different from the $C \neq 0$ case, with a larger slope. The green dashed line on the logarithmic density graph plots $P(s) = e^{-1.6\cdot(s-0.6)/\langle s \rangle}$ to approximate

the exponential portion of the data. The faster decay rate likely results from the larger average separations for this scenario. The exponential approximation appears more suitable for this data compared to the $C \neq 0$ case, more definitively demonstrating that the Poisson-statistics of the interspersed localized states dominate the level spacing behavior of the extended states with like Chern character.

Finally, the separation statistics between $C = 0$ states appear to be an intermediary between the $C \neq 0$ and $C = +1$ scenarios. The linear plot displays that the density also increases with upwards concavity near zero, just as in the $C = +1$ case. However, the logarithmic plot levels off with a larger "nose" compared to the $C = +1$ plot. The density on the logarithmic plot appears linear and Poisson-like, with a slope somewhere between the other two cases. It is logical that Poisson-like statistics are nearly followed for these localized states, with a disruption for small separations as a consequence of interspersed extended states. Since this is at the very center of the LLL, there is a significant presence of extended states, explaining why there may be limited consecutive $C = 0$ states with very close spacing and the presence of minimal level repulsion. Still, considering the localized states comprise more than half of the density at $E = 0$, it is surprising that there is not more significant density of localized states very close to one another, as was observed with the almost perfect Poisson case near the edges of the eigenvalue spectrum. It appears that the extended states are causing the localized states to behave slightly differently in the center of the LLL compared to the edges. Further analysis of the exact ordering of states is required to understand this deviation from Poisson statistics for these localized states.

Additional level spacing analysis is presented in Appendix. A for other system sizes and window sizes.

6 Level Spacing Ratio Analysis

Another relevant statistic characterizing eigenvalue spectra is the ratio of consecutive level spacings, r,

$$r_i = \frac{\min(E_i - E_{i-1}, E_{i+1} - E_i)}{\max(E_i - E_{i-1}, E_{i+1} - E_i)} = \frac{\min(s_i, s_{i+1})}{\max(s_i, s_{i+1})}, \tag{13}$$

where the eigenvalues are ordered and i is an index variable [5, 14]. Analysis of the ensemble-averaged $\langle r \rangle$ is often used for understanding and analyzing systems with a delocalization-localization transition [5]. Eigenvalues following GUE statistics should theoretically attain $\langle r \rangle = 0.5996$ while eigenvalues following Poisson statistics should attain $\langle r \rangle = 2\ln 2 - 1 = 0.3863$ [14].

Level spacing ratios are analyzed for a system of $N_\phi = 2048$ states with symmetrized data. For simplicity, each r-value is associated with the eigenvalue E_i from Equation 13 so their relationship may be plotted. Various Chern configurations are also analyzed. Eigenvalues are first filtered according to the Chern condition, the r-values are computed for the eigenvalues in each trial, and the data is finally accumulated for the entire ensemble. Fig. 7 displays 2D hexagonally binned density plots of the r-values, demonstrating the distribution of r-values over the eigenvalue spectra. Regions of brighter yellow indicate higher density of r-values. The red average curves are computed by splitting the cumulative dataset of eigenvalues into quantiles and finding the average r-value within each quantile. The first and last data point represent 0.25% of the dataset each, isolating any potential deviation at the edges of the eigenvalue spectrum. Then, 35 central quantiles are used such that each central data point contains around 2.84% of the data. For simplicity, each $\langle r \rangle$ is plotted at the midpoint between its eigenvalue bounds. The error bars are all comparable or smaller than the marker size.

For the all Chern scenario, the average r-value at the center of the band precisely reaches the GUE value. This indicates the dominating presence of level repulsions at the band center with these states of mixed Chern character. Despite the majority of states at $E = 0$ actually being localized with $C = 0$, the system follows the GUE statistics due to the strong overlap and repulsions of extended states. The color-coded density demonstrates that the density of r-values at the LLL center is highest right in the neighborhood of the dashed green line. There is also significant density up until $r = 1$ at the band center, indicating that consecutive eigenvalues typically have consistent level spacings in this region. Moving towards the edges of the energy band, the average r-values smoothly decrease until exactly reaching the Poisson value. The density appears to smear outwards from the center of the plot, and there is still significant concentration of r-values well below the Poisson limit. This demonstrates that although the average attains the Poisson value, there is considerable variation in r-values. There is very little density below the Poisson limit at the

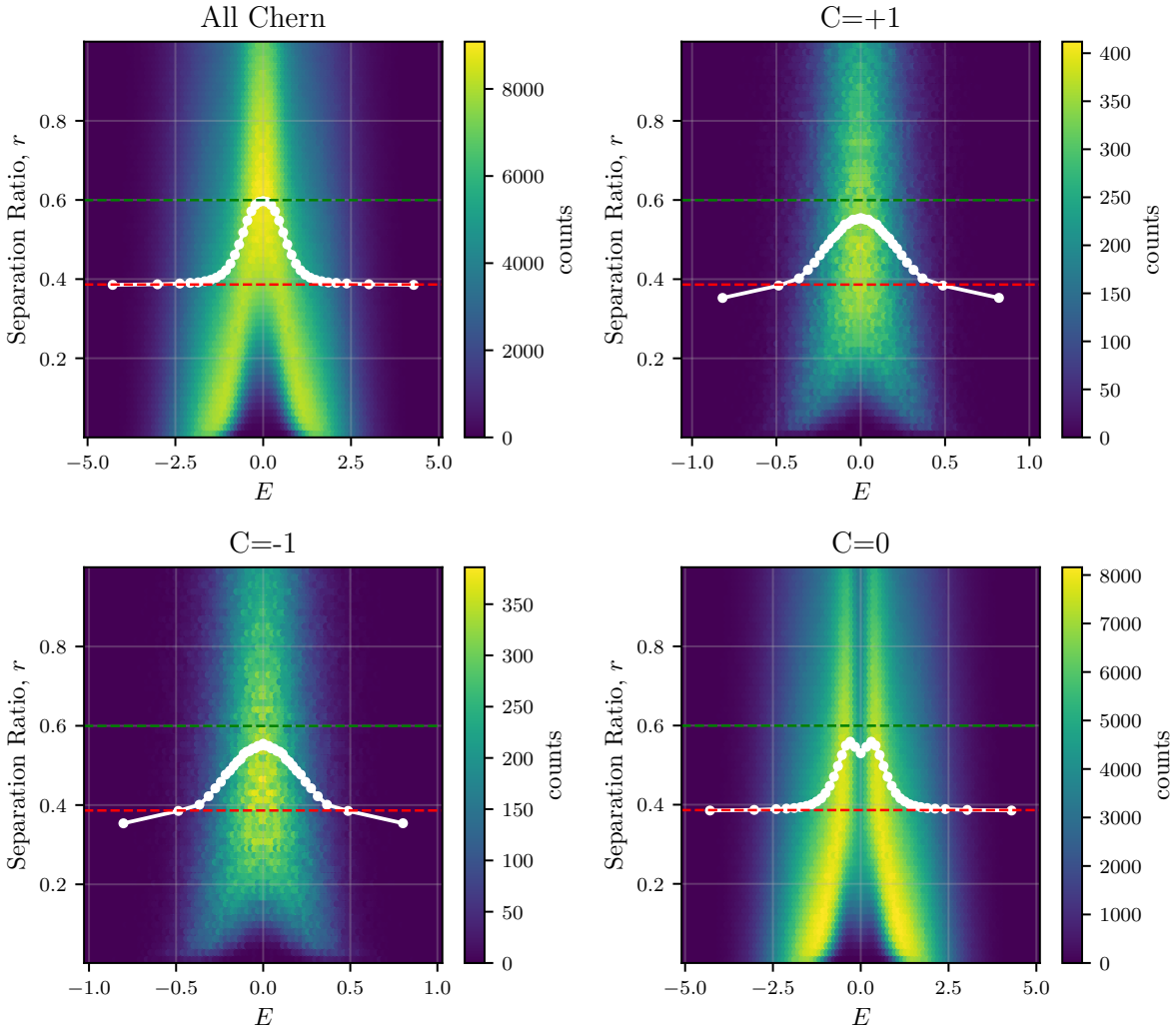

Figure 7: Hexagonal binned density plots of the level spacing ratio r versus energy E for $N_\phi = 2048$, separated by various Chern filters. Color indicates the density within each hexagonal bin. The dashed green line shows the GUE value and the dashed red line shows the Poisson value. The solid white curve represents the quantile-averaged $\langle r \rangle$ value as a function of energy.

band center, where the extended states are concentrated. As the character of the states transitions to a larger degree of localized states, the density shifts to lower r-values indicating more inconsistently spaced eigenvalues. Thus, this transition of average r-values very robustly depicts the transition between the two types of statistics in the LLL.

The $C = +1$ and $C = -1$ plots display essentially identical behavior. There is the most significant density of r-values at the center of the band between the two statistical limits, in a shape resembling a blurred arrow-head. This indicates that the extended states with identical Chern character vary significantly in their spacings. The average at $E = 0$ does not reach the GUE value, but rather an

intermediate value around $\langle r \rangle \approx 0.55$. The apparent suppression of level repulsion likely results from intervening localized states separating the extended states, as well as intervening extended states of different Chern character. Moving slightly away from the band center, the average r-value of the extended states does reach the Poisson value. This coincides with the diminishing fraction of extended states, demonstrating that the higher density of interspersed localized states begin to dominate the statistics for the sparsely distributed extended states. The very edges of the data slightly undershoot the Poisson value, although this may be a result of the extremely low concentration of data in these areas, indicated by the very dark background color.

The plot for the $C = 0$ localized states presents the most interesting scenario. The density plot indicates two curves of highest concentration in yellow beginning around $E = \pm 2.5$ at $r = 0$ until increasing to $r = 1$ against vertical asymptotes surrounding $E = 0$. There is the lowest fraction of localized states compared to extended states at $E = 0$, although, localized states are still the majority here. This density gap where there is significantly less r-data results in a dimple at the center of the average curve. The left and right peaks in the average curve attain a similar $\langle r \rangle \approx 0.55$, and the localized states at the edges of the band are at the Poisson value. The Poisson statistics are expected at the edges, but this central behavior and intermediate statistics require further analysis. The interspersed extended states between $C = 0$ states exhibit enough repulsion to influence the statistics of localized states at the LLL center. As the density of extended states decreases, the statistics return to the expected Poisson behavior. The dimple is unexpected, with the mean r-values first increasing to reach a maxima before decreasing. It is interesting that the $C = +1$ and $C = -1$ plots remove density of r-values from the center of the band, forming the gap in density of r-values for $C = 0$.

The separation ratios are also analyzed for various system sizes, reinforcing the pattern that extended states become more concentrated at the band center as the system sizes increase. The curves presented in Fig. 8 all represent the average r-values, utilizing the same quantile-binning strategy and bin sizes as previously. Error-bars are omitted for visual clarity, but a copy of the figure with error-bars is presented in Appendix B.

In the plot for all Chern states, all of the systems plotted neatly approach the GUE value at the center of the energy spectrum, demonstrating the dominant behavior of extended states. Moving

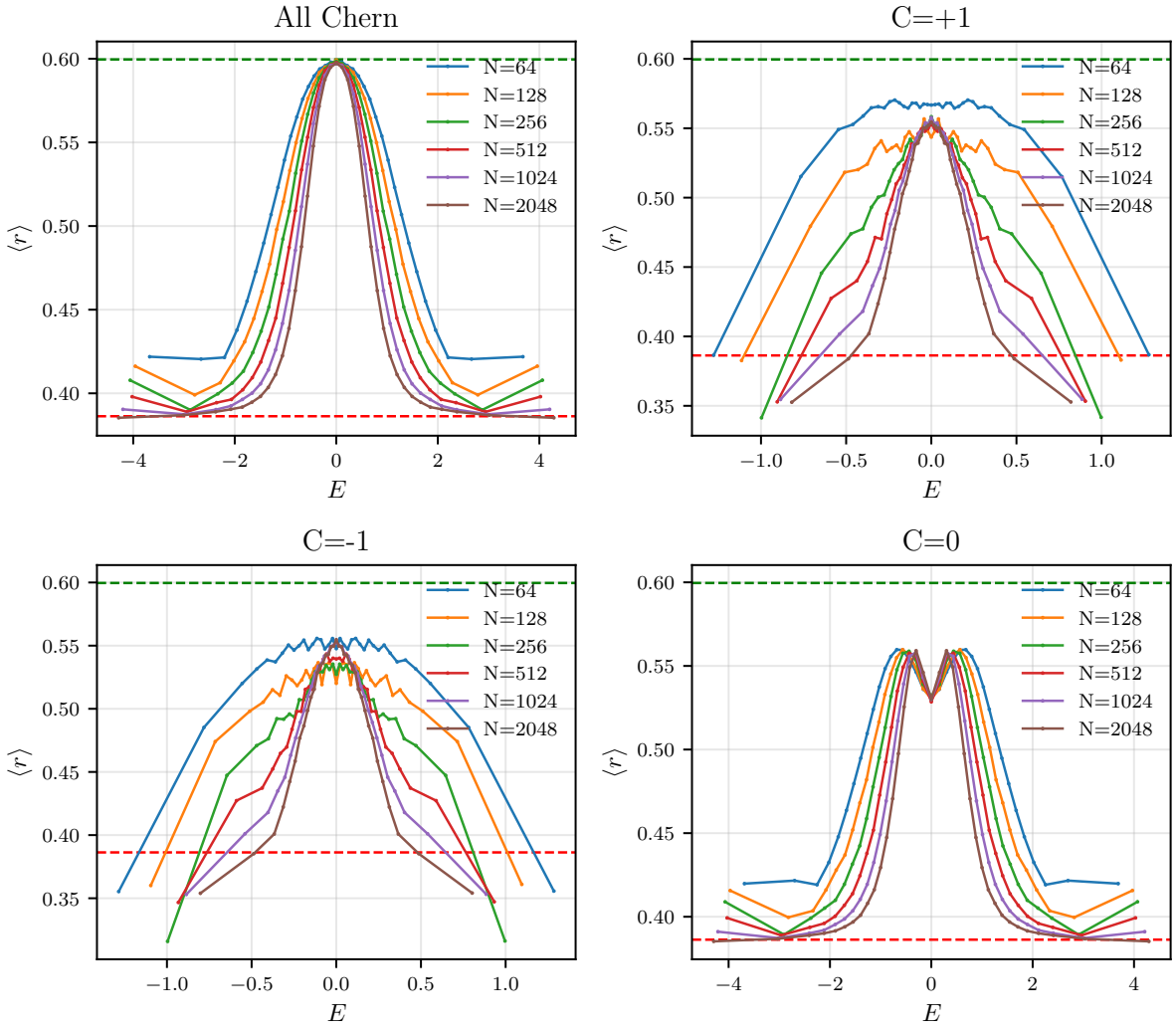

Figure 8: Average level spacing ratio $\langle r \rangle$ as a function of energy E for various system sizes, separated for various Chern conditions.

outwards, the average r-values decrease toward the Poisson value. The larger system sizes approach the Poisson value at a faster rate than the smaller systems. This indicates that the larger systems more quickly transition from GUE to Poisson statistics, consistent with the fact that the extended states become more concentrated at the center of the band with increasing system size. The average r-values for system sizes $N_\phi < 512$ do not reach the Poisson limit or slightly increase at the edges of the band: this likely results due to limited data in these regions, as well as finite-size scaling effects which are especially noticeable for the $N_\phi = 64$ system.

The $C = +1$ and $C = -1$ cases are similar to each other with some slight differences and oscillations resulting from the finite data for these extended states and the binning of data. The

$C = 1$ plot is slightly more robust and will be used for analysis, since there is more data here especially for the smaller systems. With the exception of $N_\phi = 64$, the curves all have peaks around 0.55 at the band center. The smallest system $N_\phi = 64$ is quite flat at the center, indicating that the extended states occupy a sizable amount of the energy band with significant density. As the system size increases, the curves are less flat and drop off quicker to the Poisson value. Again, this indicates that the larger systems more quickly transition to Poisson statistics, while the increased spread of extended states for smaller systems slows the transition of statistics. The smaller systems have a greater dominance of level repulsions in the energy band as a consequence of the higher proportion and spread of extended states.

The $C = 0$ curves are similar to the $N_\phi = 2048$ data, all displaying a dimple at the center and subsequent peaks slightly above $\langle r \rangle \approx 0.55$. The large systems approach the Poisson limit most quickly, mimicking the behavior seen in the all Chern plot. The maxima of the smaller systems are pushed further outward from the center, reflecting the increased localization-length.

7 Conclusion

This report implements a highly-optimized simulation pipeline for collecting eigenvalues and their corresponding Chern numbers for a two-dimensional system of non-interacting electrons under high magnetic field and a Gaussian white noise potential. A significant dataset is collected for system sizes between $N_\phi = 8$ and $N_\phi = 2048$, with a localization-length exponent $\nu = 2.483$ in experimental agreement with past studies [13]. The experimental results conclude that in the thermodynamic limit, extended states all collapse to $E = 0$ and comprise a finite fraction of the overall density of states. Localized-states at the edges of the eigenvalue spectrum are found to follow Poisson statistics, confirmed with Kolmogorov–Smirnov testing. At the center of the eigenvalue spectrum of the LLL, the level spacing statistics are highly dependent on the Chern-character of the states under analysis. For the level spacings irrespective of Chern number, the distribution seems to nearly indicate GUE statistics. Other Chern configurations seem to display Poisson-like statistics for the level spacings between similar states, likely as a consequence of interspersed states with varying Chern characters and the dominance of localized states. Level-

repulsions are present between extended states in the $C \neq 0$ case, while localized states are also unlikely to be found arbitrarily close to one another in this region as a consequence of interspersed extended states. The level spacing ratios r between all eigenvalues indicate a transition between GUE statistics at the center of the LLL to Poisson statistics at the band edges. When narrowing in on the r-statistics of specific Chern states, the results are more complex, attaining intermediate values at the band center not quite at the GUE value and approaching the Poisson limit at the band edges. While states collectively depict a clear transition between GUE and Poisson statistics, distinct Chern states exhibit more complex transitions and a mixing of statistics resulting from interspersed states of varying localization and Chern character.

This report likely raises more questions than it answers regarding the various statistics of level spacings with regard to Chern number. Only a limited number of scenarios and metrics are analyzed in this report. Still, this preliminary study demonstrates that the connection between RMT and the topological Chern number is an interesting subject for future exploration. This includes more detailed analysis of the specific functional forms of the level spacing distributions under different Chern conditions, as well as analysis of the spacing between like Chern states in terms of number of states rather than energy separations, to provide deeper insights. Ultimately, with a better understanding of the statistics relevant for different combinations of identical and varying Chern states, a simplified model may be developed in an attempt to re-create the distributions of energy values and Chern numbers for larger systems. This may be accomplished without the requirement of extremely time-consuming simulations which are infeasible for systems much larger than $N_\phi = 2048$ states in the current form. Regardless, further analysis will require the accumulation of more experimental data, building upon the current database.

Acknowledgements

I thank Professor Bhatt for the countless helpful discussions and insights, guiding me through this project and discussing new results weekly. I also thank Rhine Samajdar for his intuitive explanations about the subject and his technical guidance. The simulations presented in this report were performed on computational resources managed and supported by Princeton Research Computing, a consortium of groups including the Princeton Institute for Computational Science and Engineering (PICSciE) and Research Computing at Princeton University.

A Extended Analysis of Level Spacings

This Appendix presents additional figures and plots of eigenvalue separation data for a few additional scenarios. First, data with various window sizes will be presented for the $N_\phi = 2048$ system. Then, data for $N_\phi = 1024$ will be presented, for completeness.

A.1 Varying Window Sizes for $N_\phi = 2048$

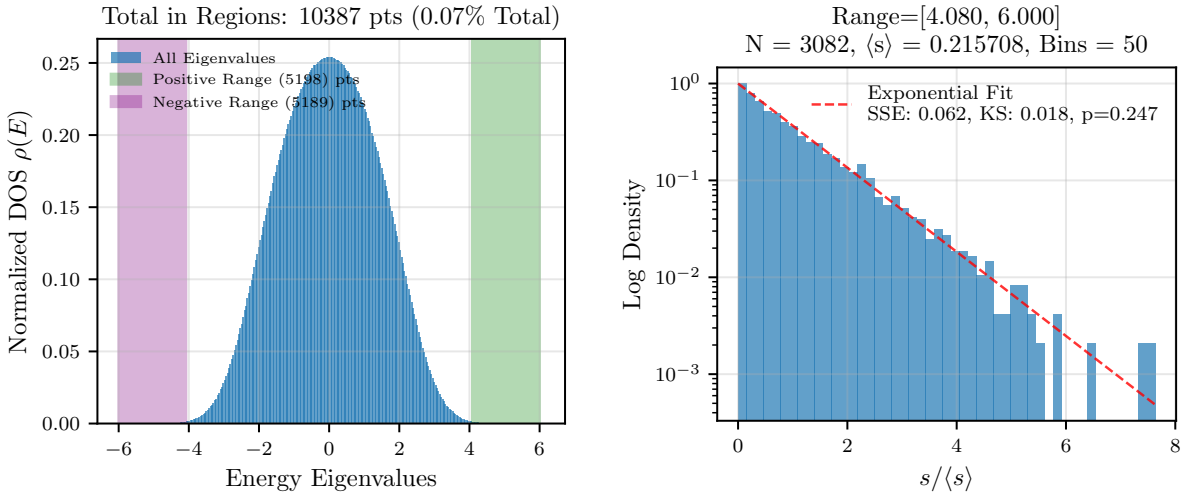

Figure 9: (A) Normalized density of states $\rho(E)$ for a system of size $N_\phi = 2048$, with two symmetric energy windows (green and magenta) highlighted. (B) Logarithmic density of normalized level spacings $s/\langle s\rangle$ for eigenvalues within the highlighted energy windows. The red dashed line shows an exponential fit $P(s) = e^{-s/\langle s\rangle}$, characteristic of Poisson statistics.

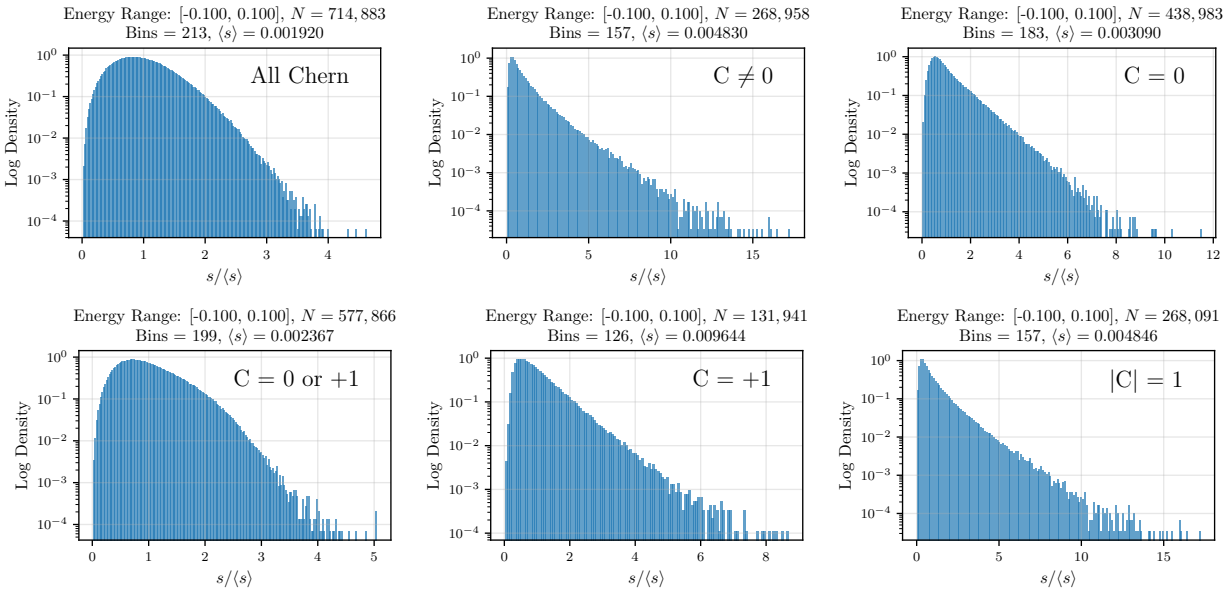

Figure 10: Normalized level spacing $s/\langle s \rangle$ distributions for eigenvalues within the central energy window $[-0.1, 0.1]$ for a system of size $N_\phi = 2048$. Each panel shows results filtered by Chern number, with the total number of level spacings N, bin count, and mean spacing $\langle s \rangle$ indicated above each plot.

Fig. 9 presents the separation data for the eigenvalues at the very edges of the eigenvalue spectrum where only 0.07% of data is contained. Compared to Fig. 5, these eigenvalues are further into the tails and are much more sparsely distributed with larger average separations. Still, these localized states very closely follow the same Poisson distribution, now with an even higher p-value of $p = 0.247$, again failing to reject the null-hypothesis. This stronger p-value likely results from the decrease in the number of separations, this time only $3{,}082$ which is less than one separation data point per trial. This results since most trials may only have a single eigenvalue in these data ranges, not enough the compute a level spacing. This confirms that the data in different portions of the tails independently follow the Poisson distribution with statistical validation.

The level spacing statistics are now presented at the center of the energy spectrum for two new window-sizes. For brevity, only the logarithmic plots are produced here. The first scenario, Fig. 10 is an approximately $3\times$ larger central window than presented previously in Fig. 6. These level spacing distributions are almost identical, with a few minor differences. The logarithmic density plots for $|C| = 1$ and $C \neq 0$ have a larger "nose" and curved portion for small separations. This "nose" decreases in magnitude as the window size is refined.

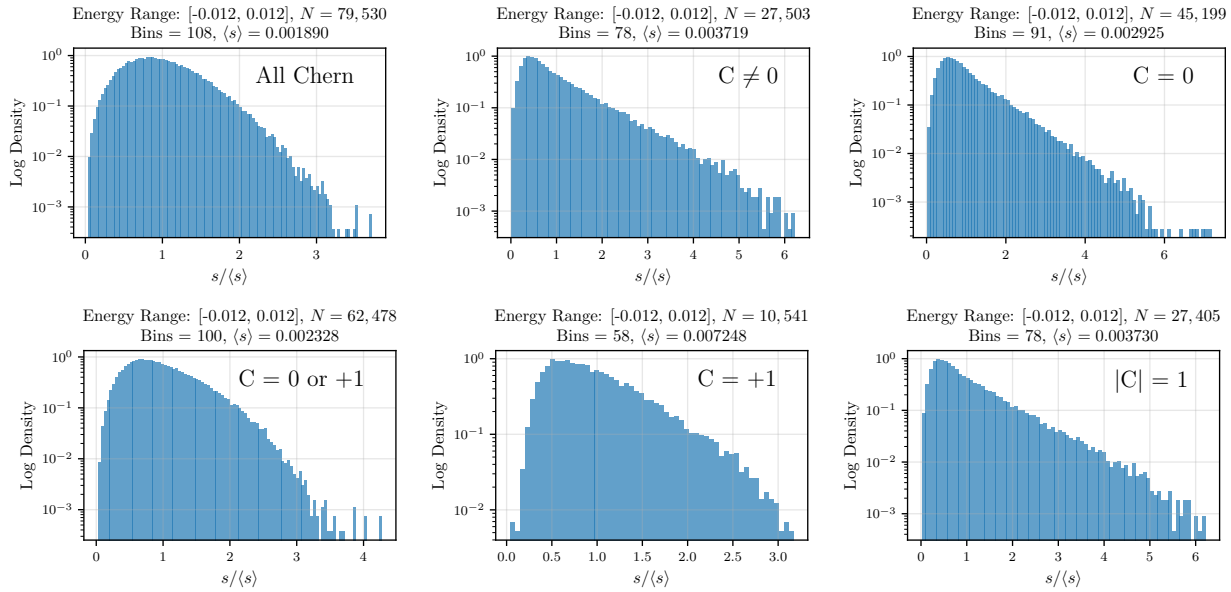

Figure 11: Normalized level spacing $s/\langle s \rangle$ distributions for eigenvalues within the central energy window $[-0.012, 0.012]$ for a system of size $N_\phi = 2048$. Each panel shows results filtered by Chern number, with the total number of level spacings N, bin count, and mean spacing $\langle s \rangle$ indicated above each plot.

The second scenario is a central window that is a third the central window size presented previously in Fig. 6. The major difference is in the $C = +1$ plot: the logarithmic density plot appears to quickly fall off for larger separations. While the plots for larger window-sizes undoubtedly depicted Poisson-like behavior of these level spacings due to the large quantity of interspersed localized states, this demonstrates that the $C = +1$ extended states approach GUE statistics nearest to the band center. However, this may be a consequence of the extremely confined window-size and lack of data, rather than the underlying statistics. This will be re-visited in the $N_\phi = 1024$ section where more data is available for study.

A.2 Separation Analysis for $N_\phi = 1024$

Almost double the total number of eigenvalues are present for this system size compared to $N_\phi = 2048$, so the data should be extremely robust and the statistics should be similar to the $N_\phi = 2048$ case. Fig. 12 displays the eigenvalue separation distributions for two window-sizes at the edges of the eigenvalue spectrum for the $N_\phi = 1024$ system. The narrow window in Fig. 12a yields an extremely robust exponential fit for the bulk of separations until the density of data falls off for large

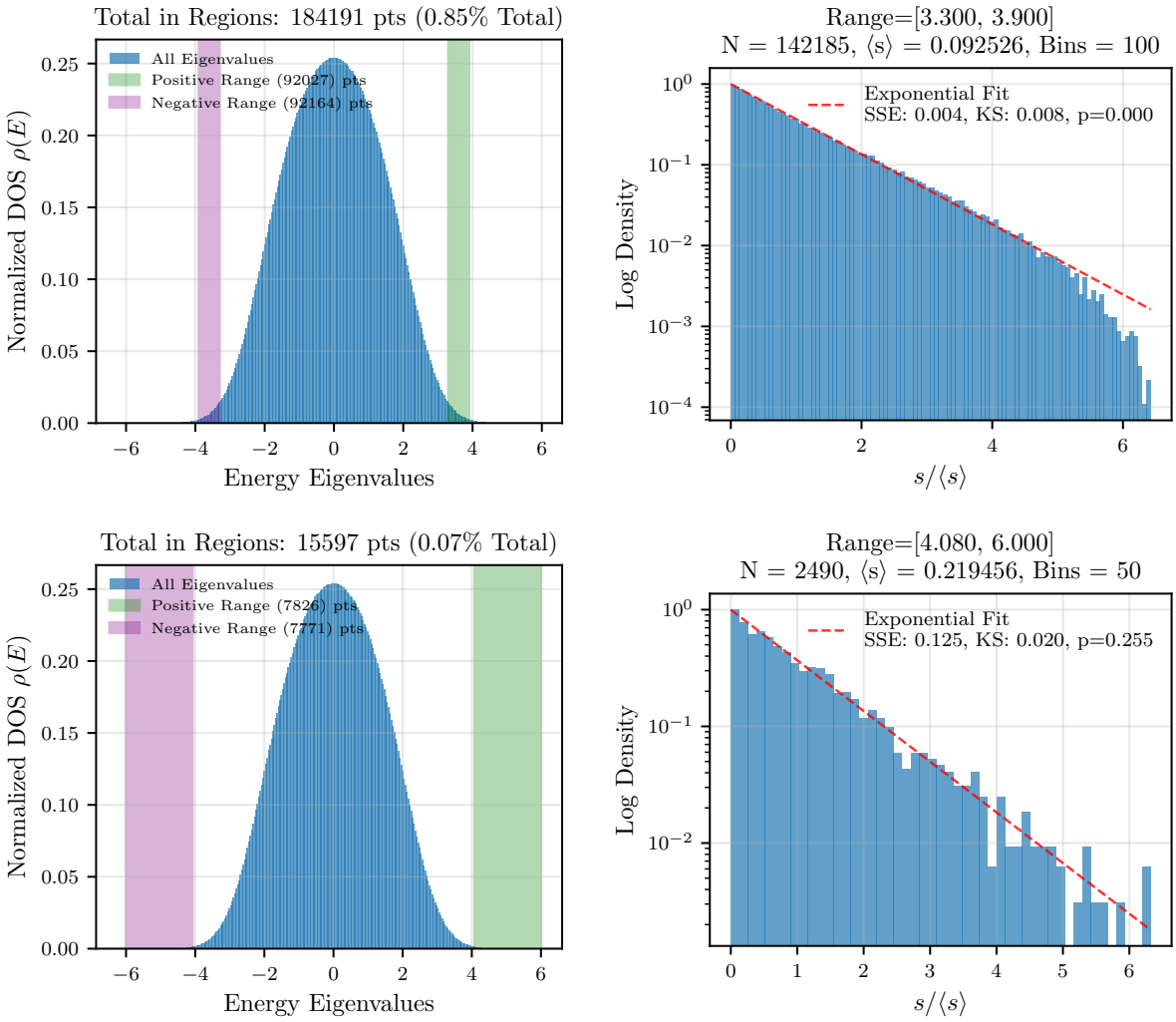

Figure 12: Logarithmic density of normalized level spacings $s/\langle s\rangle$ for eigenvalues within the highlighted energy windows for a system of size $N_\phi = 1024$. The red dashed lines shows an exponential fit $P(s) = e^{-s/\langle s\rangle}$, characteristic of Poisson statistics.

separations due to the finite window size. The p-value near 0 results due to the extremely large quantity of data, yielding statistically inconclusive results for this distribution. The windows in the tail region again robustly depict Poisson statistics for these localized states, with a p-value of $p = 0.255$ failing to reject the null-hypothesis, confirming that the data is truly Poisson distributed.

Next, the logarithmic density plots for level spacings at the center of the spectrum are displayed in Fig. 13 for a narrower window-size compared to Fig. 6, as a consequence of the larger dataset size. For the most part, these plots are identical to those observed with $N_\phi = 2048$, with two slight exceptions. The $C \neq 0$ and $|C| = 1$ plots again appear Poisson-like: however, the logarithmic den-

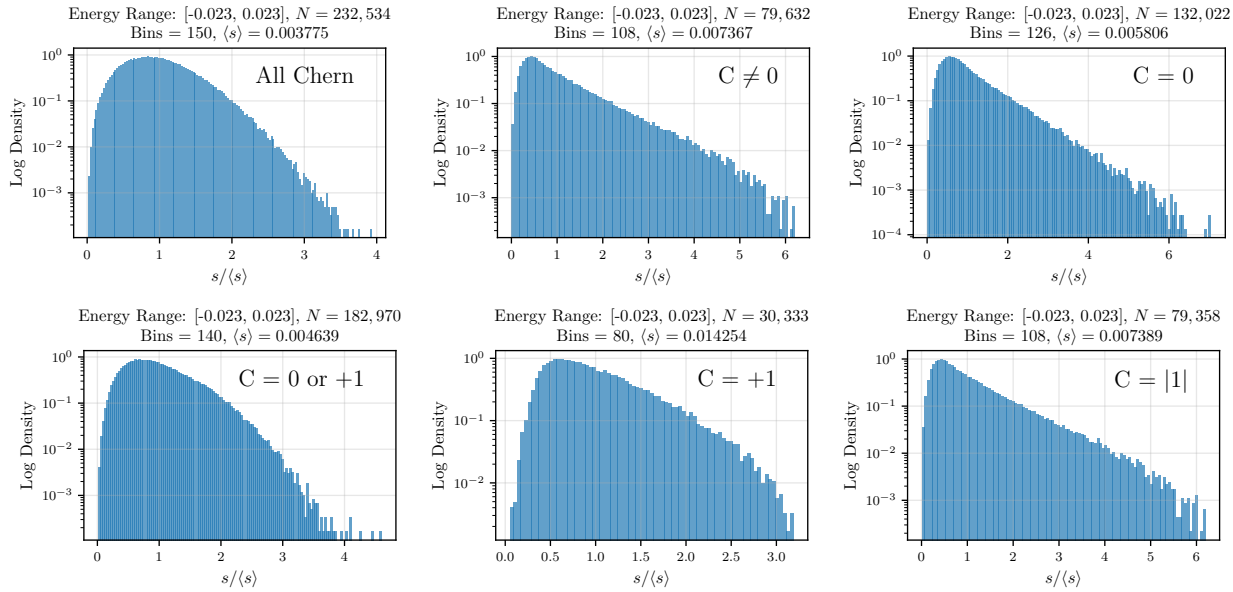

Figure 13: Normalized level spacing $s/\langle s \rangle$ distributions for eigenvalues within the central energy window $[-0.023, 0.023]$ for a system of size $N_\phi = 1024$. Each panel shows results filtered by Chern number, with the total number of level spacings N, bin count, and mean spacing $\langle s \rangle$ indicated above each plot.

sity slightly falls off in each of the tails. This data is inconclusive, and this may be a result of the finite-sized windows with low data concentration. It may be suggestive, however, of a transition to more GUE-like statistics for the extended states as a consequence of less interspersed localized states closer to the band center. The $C = +1$ plot indicates the same curving shape of the narrow-window plot observed in Fig. 11, this time with significantly more data confirming the trend. While there are only $1.5\times$ as many $C = +1$ level spacing data points as there are $N_\phi = 1024$ trials, this plot displays a robust trend. This demonstrates that at the *very* center of the band, where there is the smallest proportion of localized states, the like $C = 1$ states do in fact approach GUE statistics individually, departing from the Poisson-like behavior which was dominated by interspersed localized states. The level repulsions here begin to outweigh the interspersed localized states, bringing the level spacings closer to GUE statistics rather than Poisson statistics. The statistics are still a clear mixture between the two limiting cases, but it appears much more similar to the GUE case as opposed to the Poisson case. Thus, the statistics actually transition for states of similar Chern character depending on the positioning within the energy band and the distribution of states. This was previously observed with the $C = 0$ localized states and is now observed for the $C = 1$ extended states. With the collection of more experimental data, it may be possible to refine the

central window even further and demonstrate statistics even closer to the GUE case for $C = +1$ data.

B Extended Analysis of Level Spacing Ratios

A 2D density plot of the level spacing ratios is produced for $N_\phi = 64$ in Fig. 14. Compared to the $N_\phi = 2048$ density plots in Fig. 7, the regions of highest density are considerably spread out across the energy spectrum. This is logical, considering the longer localization-length for the smaller system. This is corroborated by the fact that the transition between GUE and Poisson statistics is more spread out in the all Chern scenario, and similarly the transition between intermediate-statistics and Poisson statistics in the $C = \pm 1$ and $C = 0$ cases. Notably, the gap in density around $E = 0$ is wider compared to the $N_\phi = 2048$ scenario, further spreading out the maxima.

Finally, a plot of the level spacing ratios for various system sizes is reproduced here with error bars in Fig. 15.

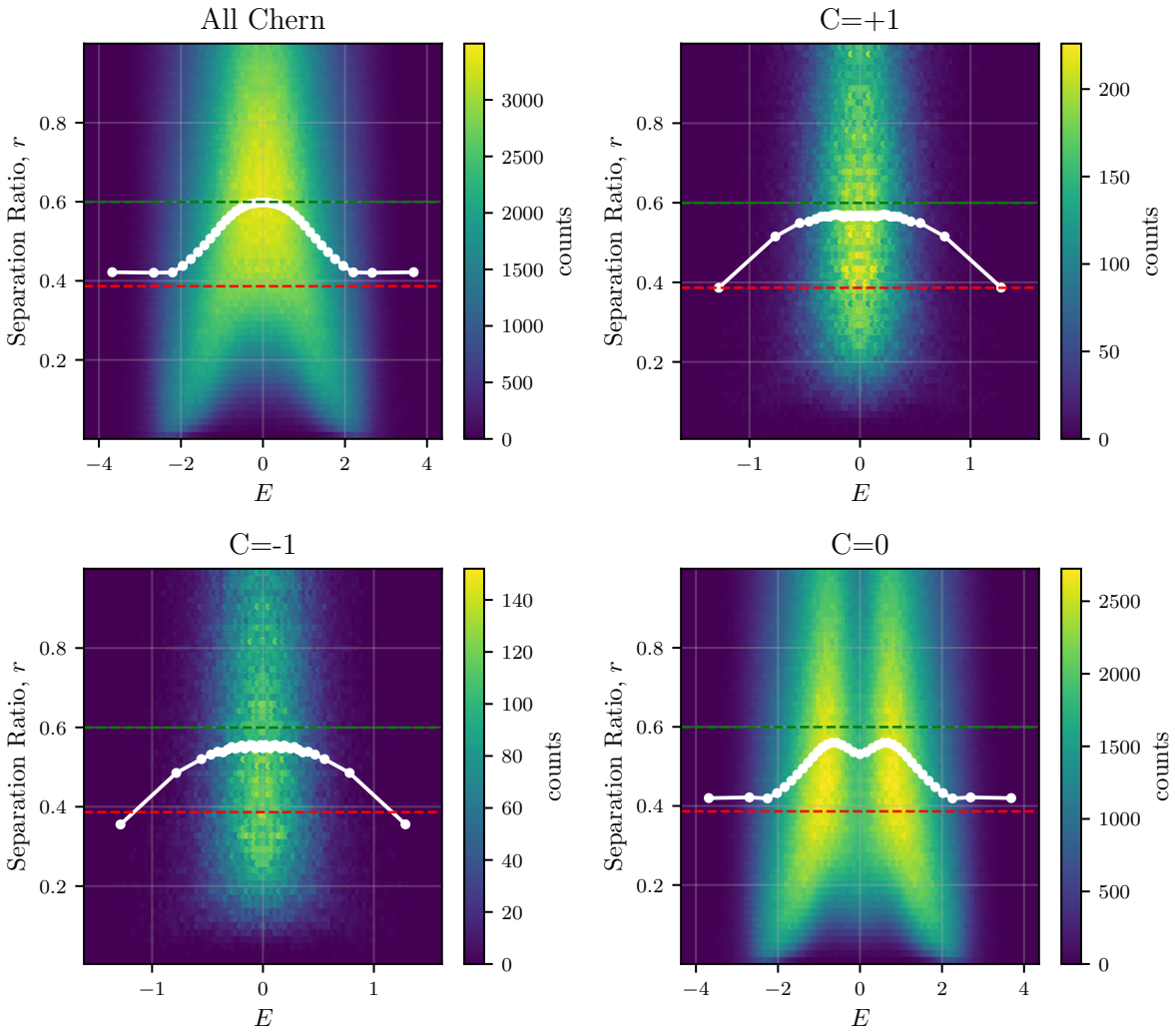

Figure 14: Hexagonal binned density plots of the level spacing separation ratio r versus energy E for $N_\phi = 64$, separated by various Chern filters. Color indicates the density within each bin. The dashed green line shows the GUE limit and the dashed red line shows the Poisson limit. The solid white curve represents the quantile-averaged $\langle r \rangle$ value as a function of energy.

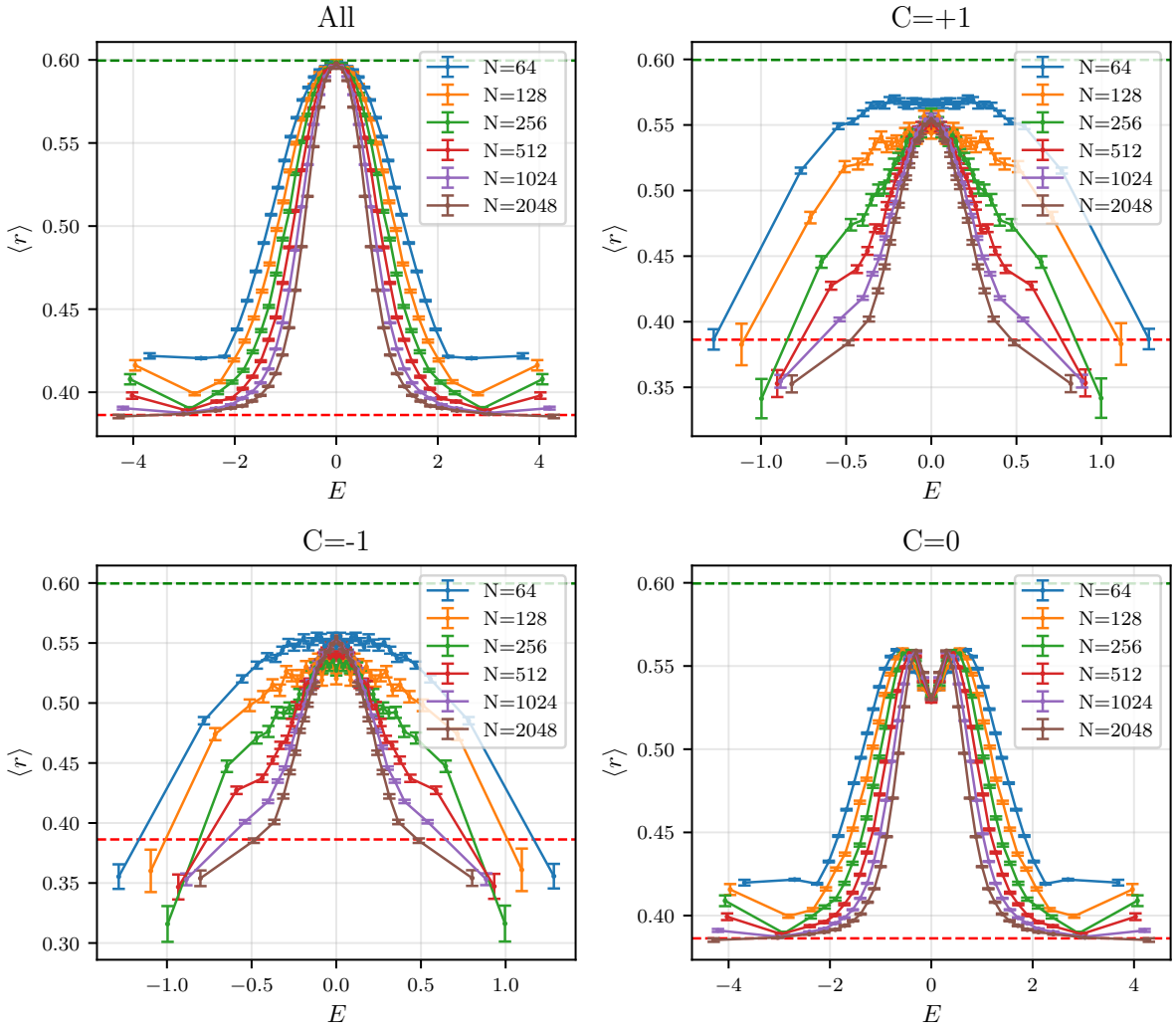

Figure 15: Average level spacing separation ratio $\langle r \rangle$ as a function of energy E for various system sizes, separated for various Chern filters.

References

[1] David Tong. *Lectures on the Quantum Hall Effect*. 2016. URL: https://arxiv.org/abs/1606.06687.

[2] N. W. Ashcroft and N. D. Mermin. *Solid State Physics*. Holt-Saunders, 1976.

[3] Klaus von Klitzing, G. Dorda, and M. Pepper. "New Method for High-Accuracy Determination of the Fine-Structure Constant Based on Quantized Hall Resistance". In: *Physical Review Letters* 45.6 (Aug. 1980). Publisher: American Physical Society, pp. 494–497. DOI: 10.1103/PhysRevLett.45.494. URL: https://link.aps.org/doi/10.1103/PhysRevLett.45.494.

[4] Klaus von Klitzing. "The quantized Hall effect". In: *Reviews of Modern Physics* 58.3 (July 1986). Publisher: American Physical Society, pp. 519–531. DOI: 10.1103/RevModPhys.58.519. URL: https://link.aps.org/doi/10.1103/RevModPhys.58.519.

[5] Akshay Krishna, Matteo Ippoliti, and R. N. Bhatt. "Localization and interactions in topological and nontopological bands in two dimensions". In: *Physical Review B* 100.5 (Aug. 2019). Publisher: American Physical Society, p. 054202. DOI: 10.1103/PhysRevB.100.054202. URL: https://link.aps.org/doi/10.1103/PhysRevB.100.054202.

[6] Daniel P. Arovas et al. "Localization, wave-function topology, and the integer quantized Hall effect". In: *Physical Review Letters* 60.7 (Feb. 1988). Publisher: American Physical Society, pp. 619–622. DOI: 10.1103/PhysRevLett.60.619. URL: https://link.aps.org/doi/10.1103/PhysRevLett.60.619.

[7] R. E. Prange. "Quantized Hall resistance and the measurement of the fine-structure constant". en. In: *Physical Review B* 23.9 (May 1981), pp. 4802–4805. ISSN: 0163-1829. DOI: 10.1103/PhysRevB.23.4802. URL: https://link.aps.org/doi/10.1103/PhysRevB.23.4802.

[8] P. W. Anderson. "Absence of Diffusion in Certain Random Lattices". In: *Physical Review* 109.5 (Mar. 1958). Publisher: American Physical Society, pp. 1492–1505. DOI: 10.1103/PhysRev.109.1492. URL: https://link.aps.org/doi/10.1103/PhysRev.109.1492.

[9] D. N. Sheng and Z. Y. Weng. "Delocalization of Electrons in a Random Magnetic Field". In: *Physical Review Letters* 75.12 (Sept. 1995). Publisher: American Physical Society, pp. 2388–2391. DOI: 10.1103/PhysRevLett.75.2388. URL: https://link.aps.org/doi/10.1103/PhysRevLett.75.2388.

[10] Y. Huo and R. N. Bhatt. "Current carrying states in the lowest Landau level". In: *Phys. Rev. Lett.* 68.9 (Mar. 1992). Publisher: American Physical Society, pp. 1375–1378. DOI: 10.1103/PhysRevLett.68.1375. URL: https://link.aps.org/doi/10.1103/PhysRevLett.68.1375.

[11] D. J. Thouless et al. "Quantized Hall Conductance in a Two-Dimensional Periodic Potential". In: *Physical Review Letters* 49.6 (Aug. 1982). Publisher: American Physical Society, pp. 405–408. DOI: 10.1103/PhysRevLett.49.405. URL: https://link.aps.org/doi/10.1103/PhysRevLett.49.405.

[12] Qian Niu, D. J. Thouless, and Yong-Shi Wu. "Quantized Hall conductance as a topological invariant". In: *Physical Review B* 31.6 (Mar. 1985). Publisher: American Physical Society, pp. 3372–3377. DOI: 10.1103/PhysRevB.31.3372. URL: https://link.aps.org/doi/10.1103/PhysRevB.31.3372.

[13] Qiong Zhu et al. "Localization-length exponent in two models of quantum Hall plateau transitions". In: *Phys. Rev. B* 99.2 (Jan. 2019). Publisher: American Physical Society, p. 024205. DOI: 10.1103/PhysRevB.99.024205. URL: https://link.aps.org/doi/10.1103/PhysRevB.99.024205.

[14] Y. Y. Atas et al. "Distribution of the Ratio of Consecutive Level Spacings in Random Matrix Ensembles". In: *Physical Review Letters* 110.8 (Feb. 2013). Publisher: American Physical Society, p. 084101. DOI: 10.1103/PhysRevLett.110.084101. URL: https://link.aps.org/doi/10.1103/PhysRevLett.110.084101.

[15] Giacomo Livan, Marcel Novaes, and Pierpaolo Vivo. *Introduction to Random Matrices - Theory and Practice*. Vol. 26. arXiv:1712.07903 [math-ph]. 2018. DOI: 10.1007/978-3-319-70885-0. URL: http://arxiv.org/abs/1712.07903.

[16] H. S. Camarda. "Statistical behavior of eigenvalues of real-symmetric and complex-Hermitian band matrices: Comparison with random-matrix theory". In: *Physical Review A* 45.2 (Jan. 1992). Publisher: American Physical Society, pp. 579–582. DOI: 10.1103/PhysRevA.45.579. URL: https://link.aps.org/doi/10.1103/PhysRevA.45.579.

[17] Isa Kh Zharekeshev and Bernhard Kramer. "Universal Fluctuations in Spectra of Disordered Systems at the Anderson Transition". In: *Japanese Journal of Applied Physics* 34.8S (Aug. 1995). arXiv:cond-mat/9506114, p. 4361. ISSN: 0021-4922, 1347-4065. DOI: 10.1143/JJAP.34.4361. URL: http://arxiv.org/abs/cond-mat/9506114.

[18] Ravindra Bhatt and Akshay Krishna. "Topology and many-body localization". In: *Annals of Physics* 435 (Dec. 2021). arXiv:2104.01635 [cond-mat], p. 168438. ISSN: 00034916. DOI: 10.1016/j.aop.2021.168438. URL: http://arxiv.org/abs/2104.01635.

[19] Yan Huo. "Numerical Studies in the Lowest Landau Level". PhD Thesis. Princeton University, New Jersey, Jan. 1993.

[20] Takahiro Fukui, Yasuhiro Hatsugai, and Hiroshi Suzuki. "Chern Numbers in Discretized Brillouin Zone: Efficient Method of Computing (Spin) Hall Conductances". In: *Journal of the Physical Society of Japan* 74.6 (2005), pp. 1674–1677. DOI: 10.1143/JPSJ.74.1674. URL: https://doi.org/10.1143/JPSJ.74.1674.

[21] Nicholas J. Higham. *Accuracy and Stability of Numerical Algorithms*. Other Titles in Applied Mathematics. Society for Industrial and Applied Mathematics, Jan. 2002. ISBN: 978-0-89871-521-7. DOI: 10.1137/1.9780898718027. URL: https://epubs.siam.org/doi/book/10.1137/1.9780898718027.

[22] Gene H. Golub and Charles F. Van Loan. *Matrix Computations*. en. Johns Hopkins University Press, 2013. ISBN: 978-1-4214-0794-4 978-1-4214-0859-0. DOI: 10.56021/9781421407944. URL: https://www.press.jhu.edu/books/title/10678/matrix-computations.

[23] Jan Carl Budich and Björn Trauzettel. "From the adiabatic theorem of quantum mechanics to topological states of matter". en. In: *physica status solidi (RRL) – Rapid Research Letters* 7.1-2 (2013), pp. 109–129. ISSN: 1862-6270. DOI: 10.1002/pssr.201206416. URL: https://onlinelibrary.wiley.com/doi/abs/10.1002/pssr.201206416.

[24] Jeffrey Heer. "Fast & Accurate Gaussian Kernel Density Estimation". en. In: *2021 IEEE Visualization Conference (VIS)*. New Orleans, LA, USA: IEEE, Oct. 2021, pp. 11–15. ISBN: 978-1-66543-335-8. DOI: 10.1109/VIS49827.2021.9623323. URL: https://ieeexplore.ieee.org/document/9623323/.

[25] Bodo Huckestein. "Scaling theory of the integer quantum Hall effect". In: *Rev. Mod. Phys.* 67.2 (Apr. 1995). Publisher: American Physical Society, pp. 357–396. DOI: 10.1103/RevModPhys.67.357. URL: https://link.aps.org/doi/10.1103/RevModPhys.67.357.

[26] Bodo Huckestein. "Scaling and Universality in the Integer Quantum Hall Effect". en. In: *Europhysics Letters* 20.5 (Nov. 1992), p. 451. ISSN: 0295-5075. DOI: 10.1209/0295-5075/20/5/012. URL: https://dx.doi.org/10.1209/0295-5075/20/5/012.

[27] Keith Slevin and Tomi Ohtsuki. "Finite size scaling of the chalker-coddington model". In: *International Journal of Modern Physics: Conference Series* 11 (Jan. 2012). Publisher: World Scientific Publishing Co., pp. 60–69. DOI: 10.1142/S2010194512006162. URL: https://www.worldscientific.com/doi/abs/10.1142/S2010194512006162.